
TensorRL-QAS: Reinforcement learning with tensor networks for scalable quantum architecture search

Akash Kundu 

QTF Centre of Excellence
Department of Physics
University of Helsinki, Finland
akash.kundu@helsinki.fi

Stefano Mangini 

QTF Centre of Excellence
Department of Physics
University of Helsinki, Finland,
Algorithmiq
stefano.mangini@helsinki.fi

Abstract

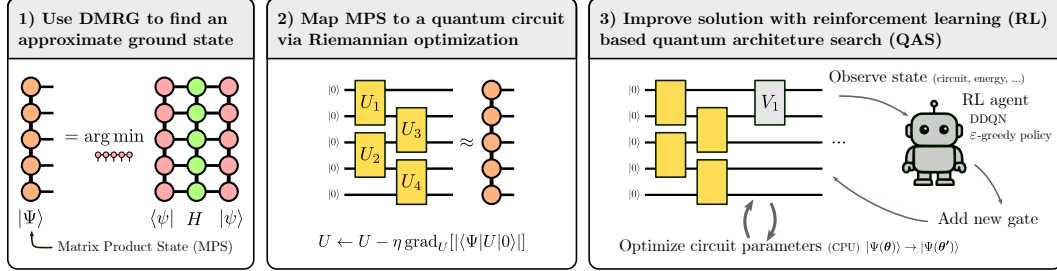
Variational quantum algorithms hold the promise to address meaningful quantum problems already on noisy intermediate-scale quantum hardware, but they face the challenge of designing quantum circuits that both solve the target problem and comply with device limitations. Quantum architecture search (QAS) automates this design process, with reinforcement learning (RL) emerging as a promising approach. Yet, RL-based QAS methods encounter significant scalability issues, as computational and training costs grow rapidly with the number of qubits, circuit depth, and noise, severely impacting performance. To address these challenges, we introduce *TensorRL-QAS*, a scalable framework that combines tensor network (TN) methods with RL for designing quantum circuits. By warm-starting the architecture search with a matrix product state approximation of the target solution, TensorRL-QAS effectively narrows the search space to physically meaningful circuits, accelerating convergence to the desired solution. Tested on several quantum chemistry problems of up to 12-qubit, TensorRL-QAS achieves up to a 10-fold reduction in CNOT count and circuit depth compared to baseline methods, while maintaining or surpassing chemical accuracy. It reduces function evaluations by up to 100-fold, accelerates training episodes by up to 98%, and achieves up to 50% success probability for 10-qubit systems—far exceeding the $<1\%$ rates of baseline approaches. Robustness and versatility are demonstrated both in the noiseless and noisy scenarios, where we report a simulation of up to 8-qubit. These advancements establish TensorRL-QAS as a promising candidate for a scalable and efficient quantum circuit discovery protocol on near-term quantum hardware.

1 Introduction

Despite the promise of quantum computing in recent years, the practical realization of quantum advantage remains elusive, primarily due to the limitations of current noisy intermediate-scale quantum (NISQ) hardware [1]. These devices are characterized by restricted qubit counts, limited connectivity, and significant noise, severely constraining the complexity of quantum circuits that can be reliably executed. As a result, most foundational quantum algorithms are not yet feasible on available quantum hardware [2], underscoring the urgent need for novel algorithmic strategies that are both effective and hardware-friendly.

To bridge this gap, hybrid quantum-classical approaches have emerged as a practical solution. Among these, variational quantum algorithms (VQAs) have become the leading paradigm for NISQ devices [3, 4, 5, 6]. VQAs operate by iteratively optimizing the parameters of a parameterized quantum circuit (PQC) to minimize a problem-specific cost function, typically the expectation value

Figure 1: **Schematic representation of *TensorRL-QAS* algorithm.** Given a Hamiltonian for which we seek the lowest eigenstate. By combining tensor network (TN) with reinforcement learning (RL)-based quantum architecture search (QAS), we find solutions that would not be achievable using either approach alone. Inspired by [12], we obtain an approximate ground state of the Hamiltonian using DMRG [13, 14], then use this result to warm-start the QAS training in RL-framework. We employ Riemannian optimization on the Stiefel manifold to map the MPS obtained from DMRG to a quantum circuit [15].



of a Hamiltonian H . In this framework, a quantum state is prepared using a PQC $U(\theta)$, the objective $C(\theta) = \langle 0 | U^\dagger(\theta) H U(\theta) | 0 \rangle$ is measured, and the parameters θ are updated via a classical optimizer to minimize the cost function. The effectiveness of VQAs heavily depends on the choice of the *ansatz* for the underlying PQCs. Typically, PQC architectures are fixed prior to optimization, often guided by hardware connectivity [7] or by problem-specific insights [3, 8, 9, 10]. While these strategies have shown early promise, the resulting circuits are often either too shallow to be expressive or too deep to be noise-resilient, thus limiting the scalability and performance of VQAs [5, 6, 11].

To address these challenges, the field has recently turned its attention to quantum architecture search (QAS) [16, 17, 18], which seeks to automate the discovery of optimal PQC structures from a finite pool of quantum gates. The goal of QAS is to identify an arrangement of gates and corresponding parameters that minimize the target cost function, thereby tailoring circuit architectures to both the problem at hand and the specific constraints of the quantum hardware. Among various QAS strategies, reinforcement learning (RL) has emerged as a particularly promising approach for navigating the vast and complex space of possible circuit architectures [19, 20, 21, 22]. In this framework, the RL-agent sequentially constructs PQCs by selecting gates and their placements, using feedback from the quantum cost function as a reward signal to guide policy updates. Despite the significant potential of RL-based QAS methods, their scalability remains a critical bottleneck. To date, most RL-driven QAS algorithms have only been demonstrated on quantum problems involving up to 8-qubit in noiseless simulations and up to 4-qubit in realistic noisy scenarios. The primary obstacles to scaling include the rapid growth of the action space with increasing qubit number and the need for longer episodes, which together demand a prohibitive number of queries to quantum simulators, let alone real quantum devices. Moreover, the computational cost of simulating quantum circuits grows rapidly with circuit depth, making QAS for larger systems exceedingly challenging (see Appendix F for a detailed discussion).

Our work is motivated by the critical need to overcome scalability limitations in RL-based quantum architecture search. To address the dual challenges of action space explosion and prohibitive simulation costs, we introduce **TensorRL-QAS**, a novel framework that combines reinforcement learning with tensor network (TN) methods for quantum architecture search. At its core, TensorRL-QAS employs a problem-aware initialization obtained with tensor networks methods, strategically initializing the search space to a physically meaningful starting point [12, 23].

Tensor network methods have become a cornerstone for scalable simulations of quantum systems, providing compact representations of complex, high-dimensional quantum states by means of an efficient representation of entanglement [24]. Their versatility and efficacy have been demonstrated in several tasks, like simulating utility-scale quantum computations [25, 26], characterizing quantum states and operations [27, 28, 29], and for quantum error mitigation [30, 31]. Following the idea originally proposed in [12, 23] on tensor network pre-training of quantum circuits, in this work, we investigate the integration of TNs and RL by warm-starting an RL-based quantum architecture search procedure with tensor network methods. We schematically summarize the main idea of the manuscript in Fig. 1.

Given an Hamiltonian for which we seek a circuit representation of the ground state, we first use DMRG [13, 14] to find a matrix product state (MPS) approximation of said ground state, then use Riemannian optimization tools to map such MPS to a quantum circuit [15], and eventually refine the circuit using RL-QAS. In particular, we test two different approaches to enhance scalability in RL-QAS: (1) *TensorRL (trainable TN-init)*, the TN warm-start is part of the RL-state, and the agent can modify its parameters while training; (2) *TensorRL (fixed TN-init)*, the TN warm-start is fixed and not part of the RL-state, so the agent cannot modify its parameters. To assess the efficacy of the methods above, we also compare against a baseline method, *StructureRL*, where the TN warm-start is replaced with a circuit having the same structure but zeroed-out parameters. While not a method of independent interest, it enables a direct comparison and demonstrates convergence with the other approaches, given sufficient training.

Through extensive benchmarks on molecular ground-state problems up to 12-qubit, both in noiseless and noisy regimes, TensorRL-QAS consistently produces more compact circuits —while maintaining or surpassing chemical accuracy— and sensibly shorten execution times, for example reducing function evaluations by up to 100-fold and accelerating training episodes by up to 98% compared to other RL-QAS methods. By integrating well-established tensor network methods into RL-based QAS, our methodology enables an effective and scalable exploration of PQC architectures, reducing the gap to a practical application of VQAs on NISQ hardware.

2 Related works

Reinforcement learning (RL) has become a prominent framework for optimizing parameterized quantum circuits (PQCs) in variational quantum algorithms, where agents are trained via tailored reward functions to select effective quantum gate sequences. Approaches such as double-deep Q-networks (DDQN) with ϵ -greedy policies have been used for ground state estimation [21], while actor-critic and proximal policy optimization methods have enabled the construction of multi-qubit entangled states [32, 33]. Deep RL has also facilitated hardware-aware circuit design and improved efficiency [20], with recent work incorporating curriculum learning, pruning [34] for QAS, and tensor decomposition for T -count minimization [35]. In the scope of benchmarking RL-based QAS, ref. [36] introduces a random agent (RA) QAS where the agent chooses the action at each step randomly from a uniform distribution in the RL-framework. Despite these advances, RL-based methods are often constrained to circuits with only a few qubits due to the exponential growth of the action space and the high computational cost per episode.

Alternative non-RL-based strategies include sampling-based methods for circuit selection in ground state estimation [16, 17], Monte Carlo sampling for PQC discovery in QFT and Max-Cut [18], and supernet-based weight sharing for quantum chemistry tasks [37]. However, these methods may suffer from noise sensitivity. Simulated annealing has also been explored for PQC optimization [38]. Meanwhile, evolutionary algorithms such as EQAS-PQC [39] have been introduced to construct PQCs more effectively. Differentiable search techniques such as quantumDARTS [40] leverage Gumbel-Softmax sampling for variational algorithms. In ref. [41], the author introduces a path- and expressivity-based training-free QAS. While these approaches expand the landscape of quantum circuit optimization, scalability and robustness remain open challenges in both noisy and noiseless settings. For a review of QAS approaches, we refer the interested readers to [42, 43].

3 Methods

In the same spirit of [12], in this work we use a tensor network to warm-start the RL-based quantum architecture search procedure (see Appendix A for a discussion on how our approach differs from previous TN and VQA synergetic methods). Specifically, we focus our investigation on problems where the goal is to find a parameterized quantum circuit that approximately prepares the ground state of a given Hamiltonian of interest. Our approach consists of three main steps, graphically depicted in Fig. 1. Given a target Hamiltonian H , the procedure goes as follows

1. Use density matrix renormalization group (DMRG) [13, 14] with a maximum allowed bond dimension χ to find a matrix product state (MPS) $|\Psi\rangle$ approximation of the ground state of H .

2. Map such MPS to a PQC $|\Psi\rangle \rightarrow U|0\rangle$ using efficient tensor network contractions and Riemannian optimization on the Stiefel Manifold [15, 44, 45].
3. Continue with RL-based QAS to add more gates to the circuit $U|0\rangle \rightarrow VU|0\rangle$ to further minimize the energy and thus better approximate the desired ground state.

Clearly, if DMRG alone accurately obtains the desired ground state, subsequent steps are unnecessary. However, if it fails at maximum bond dimension χ —a parameter that governs both the computational cost and the expressiveness of the underlying tensor network model—the solution can be improved via access to a quantum computer combined with the RL-QAS framework.

3.1 DMRG and MPS

Density matrix renormalization group (DMRG) [13, 14, 46, 47] is a well-established and arguably the most used procedure for finding ground states of quantum chemistry Hamiltonians [48]. It does so by solving the optimization problem

$$|\Psi\rangle = \arg \min_{|\psi\rangle, \|\psi\|=1} \langle \psi | H | \psi \rangle, \quad (1)$$

where $|\psi\rangle$, and hence also the solution $|\Psi\rangle$ are states modeled by a so-called Matrix Product State (MPS), which is a classically efficient parameterization of high-dimensional vectors, including quantum wavefunctions. MPS are also known as tensor trains in numerical linear algebra literature [49, 50]. An MPS for a system of n qubits can be written explicitly as

$$|\Psi\rangle = \sum_{i_1, \dots, i_n=1} A_{i_1}^{[1]} A_{i_2}^{[2]} \dots A_{i_n}^{[n]} |i_1 i_2 \dots i_n\rangle, \quad \begin{cases} A_{i_k}^{[k]} \in \mathbb{C}^{d_k}, & k \in \{1, n\} \\ A_{i_k}^{[k]} \in \mathbb{C}^{d_k} \times \mathbb{C}^{d'_k}, & k \neq \{1, n\} \end{cases}. \quad (2)$$

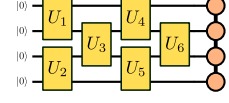
where $A_{i_1}^{[1]}$ and $A_{i_n}^{[n]}$ are row- and column-vectors, respectively, and the rest are matrices. The shapes are such that the whole vector-matrices-vector multiplication is well-defined. Importantly, all of these have size at most $d_k \leq \chi \in \mathbb{N}$. The hyperparameter χ is called *bond dimension*, and controls the amount of correlations—entanglement, in the quantum case—that the MPS can represent. The larger the bond dimension, the more expressive the model is, and thus is capable of representing more general vectors. Briefly, DMRG works by iteratively sweeping through each site in the MPS and optimizing the corresponding local matrix to minimize the cost in (1). This sweeping is continued until convergence, with the computational cost of the whole procedure scaling linearly with the number of sites and polynomially with the bond dimension χ . An in-depth explanation of DMRG and the MPS ansatz is outside the scope of this work, we refer the interested reader to [14, 46, 47].

3.2 Mapping MPS to PQC via Riemannian optimization

Given the approximate solution $|\Psi\rangle$ in MPS form, we proceed by finding a quantum circuit that prepares $|\Psi\rangle$. That is, we seek a unitary U such that $U|0\rangle \approx |\Psi\rangle$. Several proposals have been put forward to address this task, some including explicit constructions [24, 51, 52], others based on iterative variational approaches [53, 54, 55, 56]. In this work, we adopt the second approach due to its greater flexibility, hardware efficiency—it doesn’t require ancillary qubits and densely connected topologies—and better empirical performance [53, 54]. Furthermore, as the PQC will be further modified by the following RL-based QAS procedure, an approximate, rather than *exact*, reconstruction suffices. We consider unitaries U which can be decomposed as a product of 2-qubit unitaries, namely $U = \prod_{k=1}^m U_k$ with $U_k \in \text{U}(4)$. This is because most quantum computers natively implement 2-qubit interactions, and so the circuit can be mapped to real devices with minimum overhead. The actual form of the unitary U can be chosen freely, but in practice it should satisfy some requirements, like matching the topology of the quantum hardware and reducing the number of operations and depth to minimize the detrimental effect of noisy gates. In this manuscript, we restrict our attention to unitaries having a brickwork structure such as the one represented in Fig. 1. This is a well-known hardware-efficient ansatz well-suited for devices with linear connectivity [7], but we remark that other choices are possible.

The circuit can be found by maximizing the overlap between the target state $|\Psi\rangle$ and the variational model, that is maximizing the loss function

$$L(U_1, U_2, \dots) = |\langle \Psi | U | \mathbf{0} \rangle| = \left| \langle \Psi | \prod_{k=1}^m U_k | \mathbf{0} \rangle \right| \quad (3)$$



whose trainable parameters are the 2-qubit unitaries $\{U_k\}$. On the right, we show an example of a graphical representation of the tensor network representing the overlap. The minimization process is done by first constructing the overlap tensor network (3) and then using automatic differentiation to compute the gradients and update all unitaries at the same time. The contraction of the tensor network and the computation of the gradients remain efficient as long as the variational circuit is shallow enough so that the bond dimensions involved in the contraction remain controlled.

Fundamentally, the gradient-based update rule preserves the unitarity of the trainable matrices. This can be obtained employing Riemannian optimization techniques on the Stiefel manifold [44, 45, 15]. At a high-level, the procedure works by modifying the (euclidean) gradients so that the new updated matrices live on the same manifold as the starting ones. This can be done in several ways, for example, using SVD [53] or, as we instead do, with the so-called Cayley transform [44], which was shown to yield better optimization performances in many quantum-related optimization tasks [15]. Following [15], we have adapted Adam [57]) to perform Riemannian optimization on the Stiefel manifold and used it to minimize the loss (3). We refer to Appendix B for an extended discussion and technical derivations, including the full algorithm for Riemannian optimization with Adam.

3.3 Tensor-based reinforcement learning

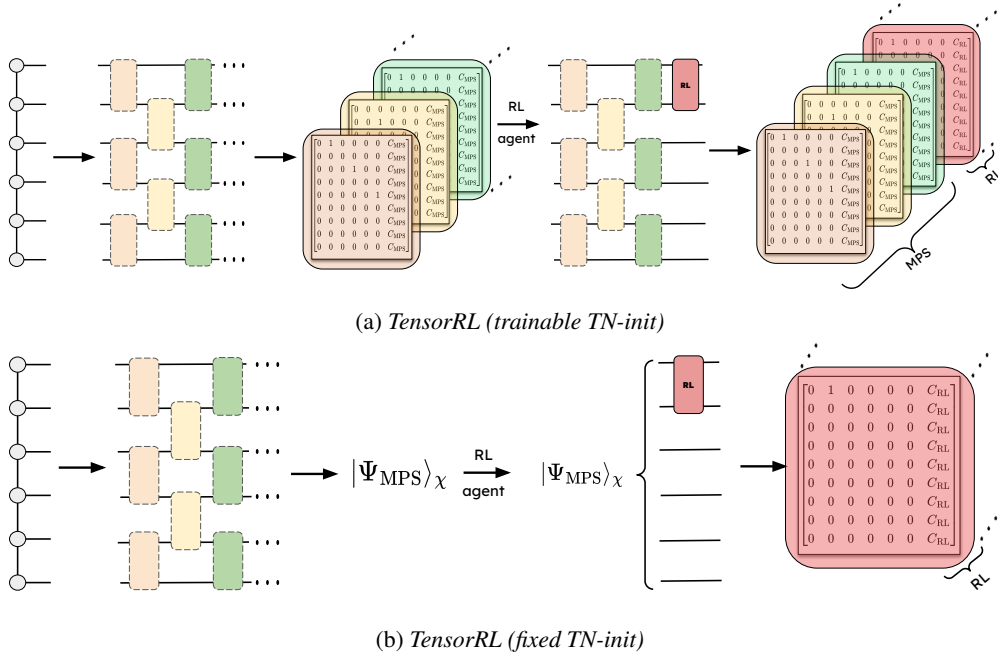


Figure 2: (a) *TensorRL (trainable TN-init)* an MPS is transformed into a brickwork circuit structure using Riemannian optimization. The circuit is encoded into a binary encoding to make it visible to the RL-agent. The RL-agent chooses a gate, and the information corresponding to the gate is encoded into a new binary matrix, highlighted in red. In contrast, in *StructureRL*, we replace the optimized parameters with zero. (b) *TensorRL (fixed TN-init)* do not directly encode the MPS structure and its parameters into the RL-state, but the empty PQC is initialized with the MPS wavefunction.

In contrast to conventional methods starting from an empty RL-state [34, 21, 20, 19], TensorRL-QAS starts from the warm-started circuit obtained using the procedures described above. The RL-agent receives such a circuit using the binary encoding scheme introduced in [34, 36]. The agent then sequentially adds gates to this initialized structure until a stopping criterion is met, for example, if the

maximum number of actions for that episode is reached, or if a target accuracy is achieved (typically, this is defined as the chemical accuracy for quantum chemistry problems). At each time step, the agent receives a modified RL-state representing the circuit with the newly proposed action. Each action is sampled from an action space containing a pool of gates, in our case set to $\{RX, RY, RZ, CNOT\}$. To steer the agent towards the target, we use the same reward function R used in [21, 34] at every time step t of an episode (see Appendix G.1 for more details). With this framework in mind, we introduce two different models, graphically represented in Fig. 2.

TensorRL (trainable TN-init) In the first method, we encode both the structure and the parameters of the warm-start circuit in the RL-state through the binary encoding, as illustrated in Fig. 2(a). This enables the agent to receive complete information regarding the MPS initialization, and trains its parameters along with ones of the newly added gates in the upcoming steps. In this setting, the size of the encoding is $(D_{\text{MPS}} + D) \times N \times (N + N_{1\text{-qubit}})$, where the first $D_{\text{MPS}} \times N \times (N + N_{1\text{-qubit}})$ encodes the MPS circuit structure of depth D_{MPS} . For each depth, the 2-qubit gates are encoded in the first $(N \times N)$ elements, and the 1-gates are encoded into the remaining $(N_{1\text{-qubit}} \times N)$ elements.

TensorRL (fixed TN-init) In the second method, illustrated in Fig. 2(b), we don’t feed the warm-start quantum circuit to the RL-state, but rather use it as a fixed initial statevector for following computations. This means that the binary encoding of the current RL-state does not contain information about the MPS state, which is indeed used here as a fixed warm-start from the RL-agent. Consequently, this reduces the size of the binary encoding tensor from $(D_{\text{MPS}} + D) \times N \times (N + N_{1\text{-qubit}})$ to $D \times N \times (N + N_{1\text{-qubit}})$. In section Sec. 4 we show that this setting significantly reduces the computational time of each episode, and this is for the following reasons: (i) due to the reduced size of the input tensor and number of steps, the quantum statevector simulation time reduces (see Appendix F); (ii) as the input tensor is an input to the neural network, reduced input size reduces the training time per step; and (iii) since the warm-start circuit is non-trainable, the number of trainable parameters in the PQC is smaller, which in turn reduces the number of energy evaluations and the time taken by the classical optimizer.

We additionally compare to **StructureRL**, a baseline where the RL agent is initialized with the warm-start circuit structure (parameters set to zero) and can add gates or modify all parameters, including those in the warm-start section; this isolates the effect of warm-starting versus fixed ansatz initialization. Both *TensorRL (fixed TN-init)* and *TensorRL (trainable TN-init)* yield the most compact PQCs among QAS baselines. With sufficient training, *StructureRL* matches the performance of *TensorRL (trainable TN-init)*, as both share the same initial structure and ultimately optimize similar parameters. Notably, *TensorRL (fixed TN-init)* accelerates episode execution, enabling efficient CPU-only training up to 8-qubit, reducing optimizer calls, and scaling RL-based QAS beyond 12-qubit, including noisy 8-qubit simulations.

4 Results

We assess the performance of TensorRL-QAS on several molecular quantum chemistry problems of size ranging from 6- to 12-qubit, specifically in finding the ground state of 6-BEH₂, 8-H₂O, 10-H₂O and 12-LiH molecules taken from [58], see Appendix G.3. We benchmark against standard RL-QAS methods including CRLQAS [34], vanilla RL-QAS [21, 36], RA-QAS [36], training-free QAS [41], SA-QAS [38] and quantumDARTS [40]. Detailed descriptions of these QAS methods can be found in Appendix C. In Tab. 1 we report results for two variants of CRLQAS, with CRLQAS (rerun) retrained under similar agent-environment settings (see Appendix G.2 for details) to other methods. Beyond quantum chemistry, Appendix E.5, we show that TensorRL-QAS outperforms baseline QAS on finding the ground state of the 5-qubit Heisenberg and 6-qubit TFIM model, delivering more compact circuits and lower error.

In all numerical experiments reported below, DMRG is run with bond dimension $\chi = 2$ (unless otherwise specified), using the implementation provided by quimb [59]. The resulting MPS is then mapped to a one-layered brickwork quantum circuit (ie, only the first three unitaries in Eq. (3)) using the procedure explained in Sec. 3.2, and then transpiled to the given pool of basis gates. The trainable parameters in the PQCs are trained using COBYLA [60] with 1000 iterations.

Table 1: TensorRL finds more compact circuit compared to CRLQAS [34], vanilla RL-QAS [21, 36], random agent (RA) QAS [36], training-free QAS [41], simulated annealing (SA) QAS [38] and quantumDARTS [40] approaches for 6-BEH₂, 8-H₂O, 10-H₂O and 12-LiH molecules. For TF-QAS [41] the total number of gates includes parameterized XX, YY and ZZ gates, which can further be decomposed into {RX, RY, RZ, CX}. NA denotes not applicable, implying that the specific data for certain variables are not available.

Molecule	Method	Error	Depth	CNOT	ROT
6-BEH ₂	TensorRL (fixed TN-init)	6.8×10^{-5}	7	5	12
	TensorRL (trainable TN-init)	6.0×10^{-5}	33	22	96
	StructureRL	5.9×10^{-5}	33	21	97
	TF-QAS [41]	1.8×10^{-3}	NA	NA	57 (total gate)
	RA-QAS [36]	5.8×10^{-4}	21	26	17
	SA-QAS [38]	5.6×10^{-3}	36	45	28
8-H ₂ O	TensorRL (fixed TN-init)	8.9×10^{-4}	6	9	15
	TensorRL (trainable TN-init)	2.0×10^{-4}	36	30	146
	StructureRL	1.3×10^{-4}	33	30	133
	CRLQAS [34]	1.8×10^{-4}	75	105	35
	CRLQAS (rerun)	1.7×10^{-4}	100	85	58
	Vanilla RL [21]	1.7×10^{-4}	96	117	48
	quantumDARTS [40]	3.1×10^{-4}	64	68	151
	RA-QAS	1.1×10^{-3}	56	87	41
	SA-QAS	2.6×10^{-3}	40	69	26
10-H ₂ O	TensorRL (fixed TN-init)	4.1×10^{-4}	17	15	17
	TensorRL (trainable TN-init, $\chi = 3$)	6.7×10^{-4}	33	34	168
	TensorRL (trainable TN-init)	7.1×10^{-4}	35	48	173
	StructureRL	5.8×10^{-4}	37	52	169
	CRLQAS (rerun)	3.4×10^{-4}	114	140	43
	Vanilla RL	2.5×10^{-4}	73	96	32
	RA-QAS	9.9×10^{-4}	80	152	58
	SA-QAS	4.7×10^{-3}	24	42	14
12-LiH	TensorRL (trainable TN-init)	1.0×10^{-2}	31	37	203
	TensorRL (fixed TN-init)	2.4×10^{-2}	15	30	9
	StructureRL	2.2×10^{-2}	40	53	179
	CRLQAS (rerun)	2.4×10^{-2}	32	68	23
	Vanilla RL	2.2×10^{-2}	140	321	94
	RA-QAS	2.3×10^{-2}	165	364	86
	SA-QAS	2.5×10^{-2}	178	390	88

4.1 Noiseless simulation

As shown in Tab. 1, *TensorRL (fixed TN-init)* consistently produces more compact circuits while maintaining competitive or better accuracy across all molecular systems. For 6-BEH₂, TensorRL (fixed TN-init) achieves 6.8×10^{-5} error with only 7 depths, 5 CNOTs, and 12 rotations—an order of magnitude improvement over RA-QAS and SA-QAS with 5-9 \times fewer CNOTs. For 8-H₂O, it requires merely 6 depth and 9 CNOTs versus 40-100 depth and 69-117 CNOTs for competing methods, while maintaining 8.9×10^{-4} error—a 7-13 \times efficiency improvement. For 10-H₂O, TensorRL (fixed TN-init) achieves 4.1×10^{-4} error with just 15 CNOTs. While vanilla RL has slightly lower error, it requires 6 \times more CNOTs and 4 \times greater depths. For 12-LiH, TensorRL (trainable TN-init, $\chi = 2$) achieves the best error using only 37 CNOTs—a 10.5 \times reduction versus SA-QAS and 8.7 \times versus vanilla RL. The fixed TN-init variant produces an exceptionally compact circuit with 15 depths, 30 CNOTs, and only 9 rotations. Moreover, TensorRL demonstrates perfect consistency, achieving chemical accuracy across 100% of seeds, while vanilla RL succeeds in only 70% of 10-H₂O trials, RA-QAS in 60%, and SA-QAS in none. TensorRL’s efficiency advantage scales with system size, growing from 5-9 \times CNOT reductions for 6-qubit systems to 10-13 \times for 12-qubit systems. Importantly, we note that the numbers reported in the Table for *TensorRL (fixed TN-init)*, only counts the operations added by the agent, which are the only ones it can see, since the warm-start is kept as a statevector and not fed to the RL-state, see Sec 3.3.

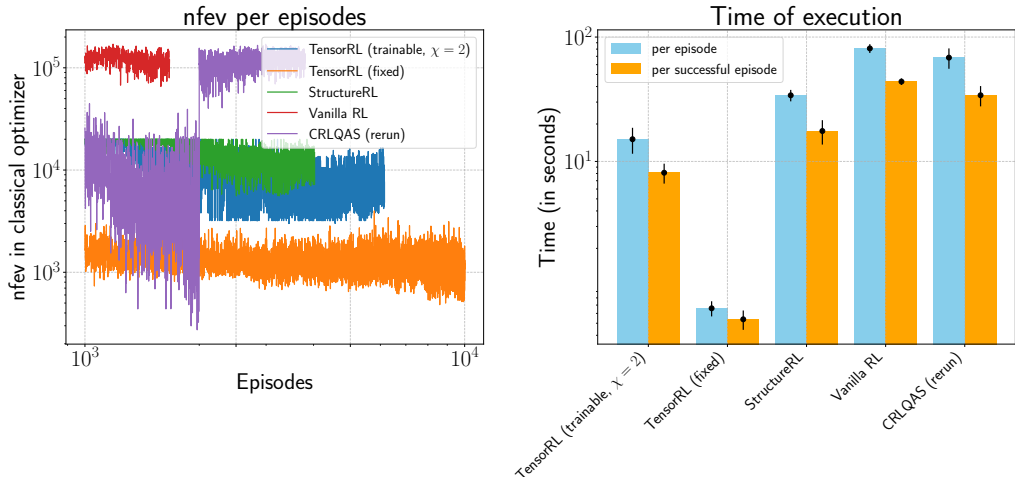


Figure 3: **TensorRL (trainable) and TensorRL (fixed) require 80% and 98% less time, respectively, to execute an episode compared to CRLQAS algorithms.** Meanwhile, TensorRL (trainable) and TensorRL (fixed) improve the number of function evaluations (nfev) by the classical optimizer by 10-100 fold, availing the corridor for more exploration-exploitation by the ϵ -greedy agent in a fixed computational budget. The error bar (on the right figure) is the standard deviation (σ) from the average over 5 random initializations of the neural network. The molecule in this example is 8-qubit H_2O .

In addition to accuracy and circuit compactness, in Fig. 3 we highlight the distinctive feature of TensorRL, namely its substantial computational efficiency. The left panel shows that *TensorRL (fixed)* consistently requires only $\sim 10^3$ function evaluations per episode, up to $100\times$ fewer than competing methods, which instead require 10^3 - 10^5 evaluations. While *TensorRL (trainable)* initially needs more evaluations, it rapidly converges to similar efficiency within 10^3 episodes. This dramatic reduction in function evaluations translates directly to lower computational overhead, as PQC simulation dominates resource usage. The right panel further underscores TensorRL’s practical gains: *TensorRL (trainable)* and *TensorRL (fixed)* reduce per-episode execution time by 80% and 98%, respectively, compared to CRLQAS. These improvements stem from TensorRL’s physically motivated initialization and exploration, which avoids expensive evaluation of suboptimal circuits. As a result, TensorRL enables more thorough exploration and optimization within the same computational budget, making it especially valuable for resource-intensive molecular simulations. Overall, the 10 – $100\times$ reduction in function evaluations and order-of-magnitude speedup establish TensorRL as both more accurate and markedly more efficient than existing PQC compilation methods.

In Appendix E.2, we show that TensorRL consistently enhances RL-agent trainability, yielding higher accumulated rewards than baselines. As problem size increases, in Appendix E.3, TensorRL maintains a success probability of up to 50%, while other methods rarely exceed 1%. These results demonstrate both the versatility and strong performance of our approach across diverse quantum systems. Additional experiments on 8- and 10-qubit CH_2O are reported in Appendix. E, which confirm the advantage of TensorRL-QAS in gate count, circuit depth, and accuracy. Fig. 6 illustrates that TensorRL-QAS converges to chemical accuracy up to 8-qubit on a CPU with better training time than CRLQAS and vanilla RL, enabling practical QAS on CPU. Finally, in Appendix. E.6 we show that with TensorRL (fixed) we can find a good approximation to the ground energy of the transverse field Ising model up to 20-qubits.

4.2 Noisy simulation

In the previous section, we ran simulations in the ideal scenario of noiseless circuit executions, and now report results for running TensorRL’s in a noisy setting. Specifically, we consider the 8-qubit H_2 molecule ground-state search problem using depolarizing noise rates exceeding current IBM quantum [61] hardware: single-qubit gate errors were amplified $10\times$, 2-qubit errors $5\times$, and shot-noise from 10^4 samples was included (see Appendix D). While these conditions do not fully

Table 2: **TensorRL outperforms baseline CRLQAS under 1- and 2-qubit depolarizing.** We tackle the problem of finding the ground state of 8-H₂O.

Noise	Method	Error	Depth	CNOT	ROT	Success prob.
Depolarizing	TensorRL (fixed)	9.0×10^{-4}	7	5	12	100%
	TensorRL (trainable)	2.48×10^{-3}	33	22	130	0%
	StructureRL	2.6×10^{-3}	28	22	129	0%
	CRLQAS (rerun)	1.3×10^{-3}	22	11	29	30%
Shot	TensorRL (fixed)	1.5×10^{-4}	3	4	1	100%
	TensorRL (trainable)	8.7×10^{-5}	30	28	131	100%
	StructureRL	6.8×10^{-4}	34	25	135	100%

capture all device-specific noise characteristics, they provide a challenging and controlled benchmark for quantum architecture search (QAS) methods. Notably, to the best of our knowledge, this is the largest simulations to date of RL-QAS in a noisy setting, which were previously limited to at most 4-qubit [37, 34]. Under these conditions, TensorRL achieved up to 38% lower variational energy error and 2.4 \times reduction in average circuit depth compared to the baseline noisy QAS method, CRLQAS [34], indicating improved resilience and scalability in both realistic and challenging noise environments.

As shown in Table 2, TensorRL (fixed) achieved chemical accuracy with 100% success rate under depolarizing noise, compared to CRLQAS’ 30% success rate at comparable error. This performance difference is linked to TensorRL’s strategy of preserving noiseless reference states during policy updates, potentially insulating the learning process from noise corruption. The method also produced shallower circuits with half of the CNOT gates compared to CRLQAS, which may help mitigate error accumulation under the amplified 2-qubit noise conditions. Under shot noise, TensorRL maintain an error below chemical accuracy with only a depth 2 circuit, though we note this simplified noise model does not account for correlated errors or crosstalk effects present in physical devices.

5 Conclusion and discussion

We introduced TensorRL-QAS, a scalable framework for quantum architecture search that combines tensor network initialization with reinforcement learning. Leveraging a matrix product state initialization, TensorRL-QAS reduces function evaluations by 100 \times and achieves 98% faster episodes compared to previous QAS approaches [41, 34, 18, 62, 38, 36], without sacrificing accuracy. For 6- to 12-qubit chemical Hamiltonians, it consistently yields circuits with 10–13 \times fewer CNOTs and depth, robust performance across random seeds, and superior efficiency and stability relative to RL and non-RL baselines. The approach generalizes to non-chemical tasks, supports CPU-only training up to 8-qubit, and maintains high accuracy under amplified noise, achieving up to 38% lower energy error and 2.4 \times smaller circuit depth than leading noisy-QAS methods. These results position TensorRL-QAS as a robust, efficient, and noise-adaptive solution for quantum circuit discovery on near-term devices.

We next outline limitations and future directions. We studied two TensorRL-QAS models: one where the warm-start is part of the RL state (and thus agent-trainable), and one where it is not. Exploring intermediate variants-e.g., where the agent observes but cannot modify the warm-start circuit- remains open. Our action space was limited to single-qubit RX, RY, RZ rotations and CNOT gates; as qubit count and problem complexity grow, richer action spaces may be required. Incorporating problem-specific (e.g., Hamiltonian-inspired) gates [16, 63, 64] or exploiting symmetries and repeated structures (e.g., gadgets [65, 66]) could improve scalability beyond 12-qubit. Appendix E.6 discusses the scalability limits of our current action set-up to 20-qubit. Finally, we always used a brickwork warm-start circuit, matching typical QPU connectivity and MPS structure; future work could examine alternative ansatzes and tensor network layouts [67, 56].

Ultimately, due to long queue times on real QPUs, our experiments rely on noise simulations, where we artificially amplify noise by 5–10 \times to test the robustness of TensorRL-QAS. However, we have not conducted training on actual quantum hardware. Future work will focus on real-device training and on developing methods to adapt TensorRL-QAS to actual QPU noise.

References

- [1] John Preskill. Quantum computing in the nisq era and beyond. *Quantum*, 2:79, 2018. 1
- [2] Thomas Monz, Daniel Nigg, Esteban A Martinez, Matthias F Brandl, Philipp Schindler, Richard Rines, Shannon X Wang, Isaac L Chuang, and Rainer Blatt. Realization of a scalable shor algorithm. *Science*, 351(6277):1068–1070, 2016. 1
- [3] Alberto Peruzzo, Jarrod McClean, Peter Shadbolt, Man-Hong Yung, Xiao-Qi Zhou, Peter J Love, Alán Aspuru-Guzik, and Jeremy L O’Brien. A variational eigenvalue solver on a photonic quantum processor. *Nature communications*, 5(1):4213, 2014. 1, 2
- [4] Jarrod R McClean, Jonathan Romero, Ryan Babbush, and Alán Aspuru-Guzik. The theory of variational hybrid quantum-classical algorithms. *New J. Phys.*, 18(2):023023, 2016. 1
- [5] Marco Cerezo, Andrew Arrasmith, Ryan Babbush, Simon C Benjamin, Suguru Endo, Keisuke Fujii, Jarrod R McClean, Kosuke Mitarai, Xiao Yuan, Lukasz Cincio, et al. Variational quantum algorithms. *Nature Reviews Physics*, 3(9):625–644, 2021. 1, 2
- [6] Kishor Bharti, Alba Cervera-Lierta, Thi Ha Kyaw, Tobias Haug, Sumner Alperin-Lea, Abhinav Anand, Matthias Degroote, Hermanni Heimonen, Jakob S Kottmann, Tim Menke, et al. Noisy intermediate-scale quantum algorithms. *Reviews of Modern Physics*, 94(1):015004, 2022. 1, 2
- [7] Abhinav Kandala, Antonio Mezzacapo, Kristan Temme, Maika Takita, Markus Brink, Jerry M Chow, and Jay M Gambetta. Hardware-efficient variational quantum eigensolver for small molecules and quantum magnets. *nature*, 549(7671):242–246, 2017. 2, 4
- [8] Andrea Skolik, Michele Cattelan, Sheir Yarkoni, Thomas Bäck, and Vedran Dunjko. Equivariant quantum circuits for learning on weighted graphs. *npj Quantum Information*, 9(1), May 2023. 2
- [9] Johannes Jakob Meyer, Marian Mularski, Elies Gil-Fuster, Antonio Anna Mele, Francesco Arzani, Alissa Wilms, and Jens Eisert. Exploiting symmetry in variational quantum machine learning. *PRX Quantum*, 4(1), March 2023. 2
- [10] Martín Larocca, Frédéric Sauvage, Faris M. Sbahi, Guillaume Verdon, Patrick J. Coles, and M. Cerezo. Group-invariant quantum machine learning. *PRX Quantum*, 3(3), September 2022. 2
- [11] Martín Larocca, Supanut Thanasilp, Samson Wang, Kunal Sharma, Jacob Biamonte, Patrick J. Coles, Lukasz Cincio, Jarrod R. McClean, Zoë Holmes, and M. Cerezo. Barren plateaus in variational quantum computing. *Nature Reviews Physics*, 7(4):174–189, March 2025. 2
- [12] Manuel S. Rudolph, Jacob Miller, Danial Motlagh, Jing Chen, Atithi Acharya, and Alejandro Perdomo-Ortiz. Synergistic pretraining of parametrized quantum circuits via tensor networks. *Nature Communications*, 14(1), December 2023. 2, 3, 14
- [13] Steven R. White. Density matrix formulation for quantum renormalization groups. *Physical Review Letters*, 69(19):2863–2866, November 1992. 2, 3, 4
- [14] Ulrich Schollwöck. The density-matrix renormalization group in the age of matrix product states. *Annals of Physics*, 326(1):96–192, January 2011. 2, 3, 4
- [15] Ilia A Luchnikov, Mikhail E Krechetov, and Sergey N Filippov. Riemannian geometry and automatic differentiation for optimization problems of quantum physics and quantum technologies. *New Journal of Physics*, 23(7):073006, July 2021. 2, 3, 4, 5, 14, 15, 16
- [16] Harper R Grimsley, Sophia E Economou, Edwin Barnes, and Nicholas J Mayhall. An adaptive variational algorithm for exact molecular simulations on a quantum computer. *Nature comm.*, 10(1):1–9, 2019. 2, 3, 9, 20, 24
- [17] Ho Lun Tang, VO Shkolnikov, George S Barron, Harper R Grimsley, Nicholas J Mayhall, Edwin Barnes, and Sophia E Economou. qubit-adapt-vqe: An adaptive algorithm for constructing hardware-efficient ansätze on a quantum processor. *PRX Quantum*, 2(2):020310, 2021. 2, 3

- [18] Shi-Xin Zhang, Chang-Yu Hsieh, Shengyu Zhang, and Hong Yao. Differentiable quantum architecture search. *Quantum Science and Technology*, 7(4):045023, 2022. 2, 3, 9
- [19] En-Jui Kuo, Yao-Lung L Fang, and Samuel Yen-Chi Chen. Quantum architecture search via deep reinforcement learning. *arXiv preprint arXiv:2104.07715*, 2021. 2, 5
- [20] Thomas Fösel, Murphy Yuezhen Niu, Florian Marquardt, and Li Li. Quantum circuit optimization with deep reinforcement learning. *arXiv preprint arXiv:2103.07585*, 2021. 2, 3, 5
- [21] Mateusz Ostaszewski, Lea M Trenkwalder, Wojciech Masarczyk, Eleanor Scerri, and Vedran Dunjko. Reinforcement learning for optimization of variational quantum circuit architectures. *Advances in neural information processing systems*, 34:18182–18194, 2021. 2, 3, 5, 6, 7, 20, 26
- [22] Owen Lockwood. Optimizing quantum variational circuits with deep reinforcement learning. *arXiv preprint arXiv:2109.03188*, 2021. 2
- [23] James Dborin, Fergus Barratt, Vinul Wimalaweera, Lewis Wright, and Andrew G Green. Matrix product state pre-training for quantum machine learning. *Quantum Science and Technology*, 7(3):035014, may 2022. 2
- [24] Aleksandr Berezutskii, Atithi Acharya, Roman Ellerbrock, Johnnie Gray, Reza Haghshenas, Zichang He, Abid Khan, Viacheslav Kuzmin, Minzhao Liu, Dmitry Lyakh, Danylo Lykov, Salvatore Mandrà, Christopher Mansell, Alexey Melnikov, Artem Melnikov, Vladimir Mironov, Dmitry Morozov, Florian Neukart, Alberto Nocera, Michael A. Perlin, Michael Perelshtein, Ruslan Shaydulin, Benjamin Villalonga, Markus Pflitsch, Marco Pistoia, Valerii Vinokur, and Yuri Alexeev. Tensor networks for quantum computing, 2025. 2, 4
- [25] Tomislav Begušić, Johnnie Gray, and Garnet Kin-Lic Chan. Fast and converged classical simulations of evidence for the utility of quantum computing before fault tolerance. *Science Advances*, 10(3), January 2024. 2
- [26] Joseph Tindall, Matthew Fishman, E. Miles Stoudenmire, and Dries Sels. Efficient tensor network simulation of ibm’s eagle kicked ising experiment. *PRX Quantum*, 5(1), January 2024. 2
- [27] Stefano Mangini, Marco Cattaneo, Daniel Cavalcanti, Sergei Filippov, Matteo A. C. Rossi, and Guillermo García-Pérez. Tensor network noise characterization for near-term quantum computers. *Physical Review Research*, 6(3), August 2024. 2
- [28] Giacomo Torlai, Christopher J. Wood, Atithi Acharya, Giuseppe Carleo, Juan Carrasquilla, and Leandro Aolita. Quantum process tomography with unsupervised learning and tensor networks. *Nature Communications*, 14(1), May 2023. 2, 16
- [29] Yuchen Guo and Shuo Yang. Quantum state tomography with locally purified density operators and local measurements. *Communications Physics*, 7(1), October 2024. 2
- [30] Sergei Filippov, Matea Leahy, Matteo A. C. Rossi, and Guillermo García-Pérez. Scalable tensor-network error mitigation for near-term quantum computing, 2023. 2
- [31] Laurin E. Fischer, Matea Leahy, Andrew Eddins, Nathan Keenan, Davide Ferracin, Matteo A. C. Rossi, Youngseok Kim, Andre He, Francesca Pietracaprina, Boris Sokolov, Shane Dooley, Zoltán Zimborás, Francesco Tacchino, Sabrina Maniscalco, John Goold, Guillermo García-Pérez, Ivano Tavernelli, Abhinav Kandala, and Sergey N. Filippov. Dynamical simulations of many-body quantum chaos on a quantum computer, 2024. 2
- [32] En-Jui Kuo, Yao-Lung L Fang, and Samuel Yen-Chi Chen. Quantum architecture search via deep reinforcement learning. *arXiv preprint arXiv:2104.07715*, 2021. 3
- [33] Esther Ye and Samuel Yen-Chi Chen. Quantum architecture search via continual reinforcement learning. *arXiv preprint arXiv:2112.05779*, 2021. 3

- [34] Yash J. Patel, Akash Kundu, Mateusz Ostaszewski, Xavier Bonet-Monroig, Vedran Dunjko, and Onur Danaci. Curriculum reinforcement learning for quantum architecture search under hardware errors. In *The Twelfth International Conference on Learning Representations*, 2024. 3, 5, 6, 7, 9, 16, 20, 26
- [35] Francisco JR Ruiz, Tuomas Laakkonen, Johannes Bausch, Matej Balog, Mohammadamin Barekatin, Francisco JH Heras, Alexander Novikov, Nathan Fitzpatrick, Bernardino Romera-Paredes, John van de Wetering, et al. Quantum circuit optimization with alphasensor. *Nature Machine Intelligence*, pages 1–12, 2025. 3
- [36] Akash Kundu, Przemysław Bedelek, Mateusz Ostaszewski, Onur Danaci, Yash J Patel, Vedran Dunjko, and Jarosław A Miszczak. Enhancing variational quantum state diagonalization using reinforcement learning techniques. *New Journal of Physics*, 26(1):013034, 2024. 3, 5, 6, 7, 9, 18
- [37] Yuxuan Du, Tao Huang, Shan You, Min-Hsiu Hsieh, and Dacheng Tao. Quantum circuit architecture search for variational quantum algorithms. *npj Quantum Information*, 8(1):62, 2022. 3, 9
- [38] Xudong Lu, Kaisen Pan, Ge Yan, Jiaming Shan, Wenjie Wu, and Junchi Yan. Qas-bench: rethinking quantum architecture search and a benchmark. In *International conference on machine learning*, pages 22880–22898. PMLR, 2023. 3, 6, 7, 9, 26
- [39] Li Ding and Lee Spector. Evolutionary quantum architecture search for parametrized quantum circuits. In *Proceedings of the genetic and evolutionary computation conference companion*, pages 2190–2195, 2022. 3
- [40] Wenjie Wu, Ge Yan, Xudong Lu, Kaisen Pan, and Junchi Yan. Quantumdarts: Differentiable quantum architecture search for variational quantum algorithms. *International Conference on Machine Learning*, 40, 2023. 3, 6, 7
- [41] Zhimin He, Maijie Deng, Shenggen Zheng, Lvzhou Li, and Haozhen Situ. Training-free quantum architecture search. In *Proceedings of the AAAI conference on artificial intelligence*, volume 38, pages 12430–12438, 2024. 3, 6, 7, 9, 17, 23
- [42] Darya Martyniuk, Johannes Jung, and Adrian Paschke. Quantum architecture search: a survey. In *2024 IEEE International Conference on Quantum Computing and Engineering (QCE)*, volume 1, pages 1695–1706. IEEE, 2024. 3
- [43] Akash Kundu. Reinforcement learning-assisted quantum architecture search for variational quantum algorithms. *arXiv preprint arXiv:2402.13754*, 2024. 3
- [44] Hemant D. Tagare. Notes on optimization on stiefel manifolds, 2011. 4, 5, 15
- [45] Nicolas Boumal. *An introduction to optimization on smooth manifolds*. Cambridge University Press, 2023. 4, 5, 15
- [46] Román Orús. A practical introduction to tensor networks: Matrix product states and projected entangled pair states. *Annals of Physics*, 349:117–158, October 2014. 4
- [47] G. Catarina and Bruno Murta. Density-matrix renormalization group: a pedagogical introduction. *The European Physical Journal B*, 96(8), August 2023. 4
- [48] Alberto Baiardi and Markus Reiher. The density matrix renormalization group in chemistry and molecular physics: Recent developments and new challenges. *The Journal of Chemical Physics*, 152(4), January 2020. 4
- [49] I. V. Oseledets. Tensor-train decomposition. *SIAM Journal on Scientific Computing*, 33(5):2295–2317, January 2011. 4
- [50] Sergey V. Dolgov and Dmitry V. Savostyanov. Alternating minimal energy methods for linear systems in higher dimensions. *SIAM Journal on Scientific Computing*, 36(5):A2248–A2271, January 2014. 4

- [51] C. Schön, E. Solano, F. Verstraete, J. I. Cirac, and M. M. Wolf. Sequential generation of entangled multiqubit states. *Physical Review Letters*, 95(11), September 2005. 4
- [52] Shi-Ju Ran. Encoding of matrix product states into quantum circuits of one- and two-qubit gates. *Phys. Rev. A*, 101:032310, Mar 2020. 4
- [53] Matan Ben-Dov, David Shnaiderov, Adi Makmal, and Emanuele G. Dalla Torre. Approximate encoding of quantum states using shallow circuits. *npj Quantum Information*, 10(1), July 2024. 4, 5, 16
- [54] Manuel S Rudolph, Jing Chen, Jacob Miller, Atithi Acharya, and Alejandro Perdomo-Ortiz. Decomposition of matrix product states into shallow quantum circuits. *Quantum Science and Technology*, 9(1):015012, nov 2023. 4, 14
- [55] Ar A Melnikov, A A Termanova, S V Dolgov, F Neukart, and M R Perelshtein. Quantum state preparation using tensor networks. *Quantum Science and Technology*, 8(3):035027, jun 2023. 4
- [56] Reza Haghsheenas, Johnnie Gray, Andrew C. Potter, and Garnet Kin-Lic Chan. Variational power of quantum circuit tensor networks. *Physical Review X*, 12(1), March 2022. 4, 9, 14, 16
- [57] Diederik P Kingma and Jimmy Ba. Adam: A method for stochastic optimization. *arXiv preprint arXiv:1412.6980*, 2014. 5, 15, 26
- [58] PennyLane. Top 20 molecules for quantum computing. <https://pennylane.ai/blog/2024/01/top-20-molecules-for-quantum-computing#2-methylene-chsub2sub>, 2025. Accessed: 2025-04-25. 6, 26
- [59] Johnnie Gray. quimb: A python package for quantum information and many-body calculations. *Journal of Open Source Software*, 3(29):819, September 2018. 6
- [60] Michael JD Powell. *A direct search optimization method that models the objective and constraint functions by linear interpolation*. Springer, 1994. 6, 18
- [61] IBM Corporation. IBM Quantum. <https://quantum-computing.ibm.com/services/resources>, 2025. Accessed: 2025-04-28. 8, 19
- [62] Hanxiao Liu, Karen Simonyan, and Yiming Yang. Darts: Differentiable architecture search. *arXiv preprint arXiv:1806.09055*, 2018. 9
- [63] Adam Glos and Özlem Salehi. A generic multi-pauli compilation framework for limited connectivity. *arXiv preprint arXiv:2412.06909*, 2024. 9
- [64] Ioana Moffic and Alexandru Paler. On the constant depth implementation of pauli exponentials. *arXiv preprint arXiv:2408.08265*, 2024. 9
- [65] Akash Kundu and Leopoldo Sarra. From easy to hard: Tackling quantum problems with learned gadgets for real hardware. *arXiv preprint arXiv:2411.00230*, 2024. 9
- [66] Jan Ollé Aguilera, Oleg M Yevtushenko, and Florian Marquardt. Scaling the automated discovery of quantum circuits via reinforcement learning with gadgets. *arXiv preprint arXiv:2503.11638*, 2025. 9
- [67] Matias Bilkis, Marco Cerezo, Guillaume Verdon, Patrick J Coles, and Lukasz Cincio. A semi-agnostic ansatz with variable structure for variational quantum algorithms. *Quantum Machine Intelligence*, 5(2):43, 2023. 9
- [68] Isabel Nha Minh Le, Shuo Sun, and Christian B. Mendl. Riemannian quantum circuit optimization based on matrix product operators, 2025. 14, 15, 16
- [69] Alan Edelman, Tomás A. Arias, and Steven T. Smith. The geometry of algorithms with orthogonality constraints. *SIAM Journal on Matrix Analysis and Applications*, 20(2):303–353, 1998. 15
- [70] Ilia A. Luchnikov, Alexander Ryzhov, Sergey N. Filippov, and Henni Ouerdane. QGOpt: Riemannian optimization for quantum technologies. *SciPost Phys.*, 10:079, 2021. 15

- [71] Hado Van Hasselt, Arthur Guez, and David Silver. Deep reinforcement learning with double q-learning. In *Proceedings of the AAAI conference on artificial intelligence*, volume 30, 2016. 17
- [72] Andrew M Childs, Eddie Schoute, and Cem M Unsal. Circuit transformations for quantum architectures. *arXiv preprint arXiv:1902.09102*, 2019. 17
- [73] Miroslav Urbanek, Benjamin Nachman, Vincent R Pascuzzi, Andre He, Christian W Bauer, and Wibe A de Jong. Mitigating depolarizing noise on quantum computers with noise-estimation circuits. *Physical review letters*, 127(27):270502, 2021. 19
- [74] Carlo Beenakker and Christian Schönenberger. Quantum shot noise. *Physics Today*, 56(5):37–42, 2003. 19
- [75] Yasunari Suzuki, Yoshiaki Kawase, Yuya Masumura, Yuria Hiraga, Masahiro Nakadai, Jiabao Chen, Ken M Nakanishi, Kosuke Mitarai, Ryosuke Imai, Shiro Tamiya, et al. Qulacs: a fast and versatile quantum circuit simulator for research purpose. *Quantum*, 5:559, 2021. 25, 26
- [76] Richard S Sutton and Andrew G Barto. *Reinforcement learning: An introduction*. MIT press, 2018. 26

A Comparison to prior TN-PQC synergistic frameworks

While both our method and the approach of Rudolph et al. [12] harness tensor networks (TNs) to enhance parametrized quantum circuits (PQCs), there are several key differences between the two works:

- **Integration with reinforcement learning and quantum architecture search:** Rudolph et al. [12] extend the quantum circuit obtained from an MPS warm-start with a fixed PQC structure initialized with random parameters, and then optimize all parameters in the circuit to further decrease the cost function. In contrast, *TensorRL-QAS* doesn’t add a fixed PQC but rather uses reinforcement learning (RL) within a quantum architecture search framework to dynamically explore and optimize the additional circuit architectures that best help in minimizing the loss. Such flexible exploration allows for a balanced search of architectural expressivity and circuit compactness, and hence noise resilience, a capability that is not present in fixed PQC schemes.
- **Trainability of PQCs vs. scalability of RL-QAS:** The main focus of [12] is to mitigate barren plateaus and improve trainability of PQCs through MPS-based initializations. On the contrary, our work focuses on alleviating the heavy computational requirements required by RL-based QAS procedures, thus making them practical also on larger system sizes. Indeed, we show that our approach can achieve *98% reduction in classical computational overhead* by warm-starting RL policies with MPS-based warm-starts.
- **Different set of basis gates:** Compared to [12], in this work we use a different and simpler set of basis gates, which is closer to operations that are natively available on hardware, and thus reducing potential compilation overheads.
- **Different MPS-to-QC mapping scheme:** In [12], the authors use a combination of explicit constructions and trainable operations to build the quantum circuit approximating the MPS warm-start [54]. In this work, instead, we use a fully variational method to find such a mapping based on Riemannian optimization [15, 56, 68].

B Mapping an MPS to a quantum circuit via Riemannian optimization

In this appendix we explain more in detail the procedure used to find a quantum circuit representation of a MPS using Riemannian optimization.

We consider the case where one fixes the *structure* of the quantum circuit, and aims to find the two-qubit unitaries that maximize the overlap with the target quantum state. Specifically, let $|\Psi\rangle$ denote the target MPS, and let $U = \prod_{k=1}^M U_k$ the unitary representing a quantum circuit with a given

structure, where each of the U_k are two qubit gates. We then want to solve the following optimization problem

$$\{U_k^*\} = \arg \min_{\{U_k\}} 1 - L(\{U_k\}), \quad L(\{U_k\}) = |\langle \Psi | U | \mathbf{0} \rangle| = \left| \langle \Psi | \prod_{k=1}^M U_k | \mathbf{0} \rangle \right| \quad (4)$$

with $U_k \in U(4) = \{U \in \mathbb{C}^4 \times \mathbb{C}^4 | U^\dagger U = U U^\dagger = \mathbb{I}_4\} \forall k = 1, \dots, M$,

that is, we want to perform optimization on the manifold on unitary matrices, the so-called complex *Stiefel manifold* (actually, we consider the simpler case of unitary matrices rather than isometries). Such problem is solved using Riemannian optimization techniques aimed specifically at solving optimization problem on manifolds [69, 45, 15, 44].

We solve the minimization problem above by adapting gradient-descent methods so that each of the trainable parameters of the cost function $L(\cdot)$, namely the matrices $\{U_k\}$, remain unitary during the whole optimization process. Our implementation largely follows [15], and we refer the interested reader to such reference for an in-depth analysis on the topic of Riemannian optimization, specifically for quantum information tasks. We note that since we are considering optimization over unitary matrices (rather than isometries), the *euclidean* and *canonical* metric on the Stiefel manifold coincide [69], which greatly simplifies the formulas, for example compared to those reported in [15]. Additionally, in order to move from one point to another on the manifold we use *Cayley's retraction*, as it was seen to improve convergence compared to other methods, based for example on SVD [15].

Let $\{U_1^t, \dots, U_M^t\}$ denote the trainable unitaries at time step t during optimization. Then, following [15, 70], an optimization procedure for adapting Adam [57] on the Stiefel manifold can be obtained as follows:

1. Start optimization ($t = 0$) from a point on the manifold, that is start with unitary matrices $\{U_1^0, \dots, U_M^0\}$ with $U_k^0 \in U(4) \forall k = 1, \dots, M$. For each of them, set the corresponding initial momentum and velocity terms to zeros

$$m_k^{t=0} = v_k^{t=0} = \mathbf{0} \quad \forall k = 1, \dots, M; \quad (5)$$

where $\mathbf{0}$ is a matrix of shape 4×4 containing zeros;

2. For $k = 1, \dots, M$, compute the (euclidean) gradients of the loss function at the current points

$$\left\{ \frac{\partial L}{\partial U_1^t}, \dots, \frac{\partial L}{\partial U_M^t} \right\} \quad (6)$$

where each of the partial derivatives is itself a 4×4 complex matrix. Importantly, since the variables are complex, the conjugate of the gradients are used in the following steps $\partial L / \partial U_k^t \rightarrow (\partial L / \partial U_k^t)^*$;

3. For $k = 1, \dots, M$, compute the Riemannian gradients given the (euclidean) gradients from the previous step (see Eq. (14) in [15])

$$\nabla_R L(U_k^t) = \frac{\partial L}{\partial U_k^t} - U_k^t \left[\frac{\partial L}{\partial U_k^t} \right]^\dagger U_k^t \quad (7)$$

4. For $k = 1, \dots, M$, compute the updated momentum and velocity terms as

$$\begin{aligned} \tilde{m}_k^{t+1} &= \beta_1 m_k^t + (1 - \beta_1) \nabla_R L(U_k^t) \\ \tilde{v}_k^{t+1} &= \beta_2 v_k^t + (1 - \beta_2) \text{Tr}[\nabla_R L(U_k^t)^\dagger \nabla_R L(U_k^t)] \end{aligned} \quad (8)$$

where $\text{Tr}[\nabla_R L(U)^\dagger \nabla_R L(U)] = \langle \nabla_R L(U) | \nabla_R L(U) \rangle$ is the inner product of the Riemannian gradients given the metric. It is the equivalent of the gradient squared term in usual Adam (see also [68]).

5. For $k = 1, \dots, M$, compute the update direction as

$$\tilde{U}_k^{t+1} = m_k^{t+1} / \left(\sqrt{v_k^{t+1}} + \varepsilon \right) \quad (9)$$

where the square root and division are meant element-wise;

6. Apply bias-correction to the learning rate $\eta \rightarrow \eta\sqrt{1 - \beta_2^t}/(1 - \beta_1^t)$;
7. For $k = 1, \dots, M$, move to another point on the manifold using *Cayley's retraction* (see Eq. (15) in [15], specialized for unitary matrices)

$$U_k^{t+1} = R_{U_k^t}^{\text{Cayley}}(-\eta \tilde{U}_k^t)$$

$$R_U^{\text{Cayley}}(V) := \left(\mathbb{I}_4 - \frac{W}{2}\right)^{-1} \left(\mathbb{I}_4 + \frac{W}{2}\right) U, \quad W = \frac{VU^\dagger - U^\dagger V}{2} \quad (10)$$

8. For $k = 1, \dots, M$, use vector transport to the momentum and velocity terms the new points on the manifold (see Eq. (16) in [15])

$$m_k^{t+1} = P_{U_k^{t+1}}(\tilde{m}_k^{t+1}), \quad v_k^{t+1} = P_{U_k^{t+1}}(\tilde{v}_k^{t+1}) \quad \text{with } P_U(V) := \frac{1}{2}(V - UV^\dagger U). \quad (11)$$

9. Repeat steps (2) to (8) until convergence.

We compute the euclidean gradients in step (2) using automatic differentiation on a tensor network representation of the loss function in Eq. (4). Alternatively, the gradients with respect to each of the unitaries can be obtained by the standard ‘‘punching a hole’’ method for computing gradients in tensor networks [28, 68]. Also, we remark that we perform a gradient-descent step on *all* unitaries in the variational circuit *at the same time*, that is we simultaneously update them in a single step of the optimization loop. Other approaches are however possible. For example, a DMRG-like optimization procedure could optimize a single unitary while keeping the remaining ones fixed, and then sweep over all unitaries until convergence [56, 53].

C QAS algorithms summary

C.1 CRLQAS: Curriculum reinforcement learning for QAS

The CRLQAS introduced in [34] integrates curriculum-based reinforcement learning with quantum circuit architecture search to address the challenges of variational quantum algorithms under hardware noise. In CRLQAS, the agent interacts with an environment where each state is a quantum circuit represented by a tensor-based binary encoding. This 3D binary-encoding captures the gate operations across qubits, circuit depth (moments), and gate types $\{\text{CNOT}, \text{RX}, \text{RY}, \text{RZ}\}$, allowing efficient processing by neural networks. The action space is defined by all possible single-qubit rotations and CNOT gates, amounting to $3N + 2\binom{N}{2}$ actions for N qubits. To reduce redundancy and improve learning efficiency, a mechanism for illegal actions is employed, which prevents the agent from appending consecutive identical gates on the same qubit or repeating the same CNOT gate, effectively pruning the action space.

A central feature of CRLQAS is its curriculum learning mechanism, which adapts the difficulty of the optimization task as the agent learns. The curriculum is governed by a moving threshold ξ that determines when an episode is considered successful. This threshold is not static; instead, it is updated based on the agent’s performance using a feedback-driven scheme. Initially, the threshold ξ_1 is set empirically. As the agent finds lower energies, the threshold is updated according to

$$\xi_{\text{new}} = |\mu - \xi_2| + \delta,$$

where ξ_2 is the best energy found so far, δ is a small amortization parameter (typically 0.0001), and μ is the so-called fake minimum energy. The fake minimum energy is calculated as

$$\mu = - \sum_i |c_i|,$$

where c_i are the coefficients in the Pauli decomposition of the molecular Hamiltonian. This value serves as a theoretical lower bound for the ground state energy, ensuring the agent is always guided towards physically meaningful solutions as guaranteed by Rayleigh’s variational principle.

The curriculum learning framework further incorporates adaptive rules: after every G episodes (e.g., $G = 500$), the threshold is greedily shifted to $|\mu - \xi_2|$, and after every 50 successful episodes, it is decreased by δ/κ ($\kappa = 10$). If the agent fails to improve the energy for 500 consecutive

episodes, the threshold is reset to $\xi_{\text{new}} + \delta$, allowing the agent to escape local minima. This dynamic adjustment ensures that the agent is neither stuck in an overly difficult regime nor allowed to stagnate at suboptimal solutions.

The agent’s exploration-exploitation trade-off is managed via an ϵ -greedy policy, where the probability of taking a random action decays exponentially from 1 to 0.05 as training progresses:

$$\epsilon(t) = \max(0.05, 0.99995^t).$$

Experience replay with a buffer size of 20,000 and double Q-network [71] architectures with periodic target updates are used to stabilize learning. To encourage the discovery of compact circuits, CRLQAS employs a random halting scheme for episodes, where the maximum episode length is sampled from a negative binomial distribution:

$$\Pr(X = n_{\text{fail}}) = \binom{n_{\text{act}} - 1}{n_{\text{fail}}} p^{n_{\text{fail}}} (1 - p)^{n_{\text{act}} - n_{\text{fail}}},$$

with n_{act} as the maximum number of actions and p the failure probability. This approach increases the likelihood of shorter, more efficient circuits being discovered early in training.

For parameter optimization within each circuit, CRLQAS uses a hybrid Adam-SPSA optimizer. This combines the robustness of simultaneous perturbation stochastic approximation (SPSA) with the adaptive momentum of Adam, and employs a multi-stage shot budget strategy (from 10^3 to 10^8 shots) for efficient convergence in noisy environments. The noise simulation leverages the Pauli-transfer matrix (PTM) formalism, with noisy gate operations precomputed offline and accelerated using JAX for GPU, yielding up to a six-fold speedup over conventional CPU-based simulations.

Empirically, CRLQAS achieves chemical accuracy (energy error below 1.6×10^{-3} Hartree) for molecules up to 8-qubit, often using fewer gates than baseline methods. The curriculum learning mechanism, driven by the fake minimum energy and adaptive thresholds, enables the agent to autonomously adjust the problem difficulty, maintain exploration, and efficiently find noise-resilient, gate-efficient quantum circuits even under realistic hardware noise profiles. This makes CRLQAS a robust and scalable approach for quantum architecture search in both idealized and practical noisy intermediate-scale quantum (NISQ) settings.

C.2 TF-QAS: Training-free QAS

TF-QAS [41] is a novel quantum architecture search (QAS) method that aims to eliminate the need for resource-intensive circuit training. It primarily contains the following two steps: (1) *Path-based proxy*: The quantum circuit is represented by a directed acyclic graph [72]. Using the path count between the input-output nodes as a zero-cost complexity metric, this step filters unpromising circuits this enabling rapid pruning of the search space. (2) *Expressibility proxy* Evaluating the remaining circuit using Hilbert space convergence

$$\mathcal{E}(C) = -D_{KL}(P_C(F) \parallel P_{\text{Haar}}(F)), \quad (12)$$

where $P_C(F)$ is the fidelity distribution of random states and P_{Haar} is Haar-random distribution. Although the progressive strategy balances efficiency in the first step and accuracy in the second,

Table 3: **TensorRL converges faster to the optimal circuit structure than TF-QAS.** The times noted for TensorRL are the average time taken by the TensorRL (trainable TN-init) and TensorRL (fixed TN-init) methods.

	Method	Training time (h)	Time to solution (h)
6-BEH ₂	TF-QAS	2.5	NA
	TensorRL-QAS	1.2	0.9

making it practical for NISQ-era quantum devices in Tab. 1, we train TensorRL-agent in finding the ground state of 6-BEH₂ and consistently achieves 100-fold better accuracy across all seeds with more quantum quantum circuit, within a smaller time as shown in Tab. 3.

C.3 RA-QAS: Random agent for QAS

Following the methodology introduced in [36]. The random agent constructs quantum circuits by selecting actions uniformly at random from the available gate set $\{\text{RX}, \text{RY}, \text{RZ}, \text{CNOT}\}$ at each step of an episode. This process is independent of the current circuit state or any reward feedback.

After each randomly selected gate is appended to the circuit, all gate parameters (e.g., rotation angles) are initialized (new gates set to zero, previous gates retain optimized values), and the entire parameter set is optimized using a classical optimizer (COBYLA [60]) to minimize the VQE cost function. This global optimization ensures a fair comparison with learning-based agents, which also rely on classical optimization for parameter updates. Each episode consists of a fixed number of steps D , corresponding to the maximum allowed circuit depth. The episode terminates early if the cost function C_t falls below a predefined threshold, i.e the chemical accuracy, indicating successful diagonalization; otherwise, it proceeds until all steps are exhausted.

Algorithm 1 Random Agent for QAS

```

1: for episode = 1 to  $N_{\text{episodes}}$  do
2:   Initialize empty quantum circuit  $\mathcal{C}$ 
3:   for step = 1 to  $D$  do
4:     Randomly select action  $a$  from the gate set RX, RY, RZ
5:     Randomly select target (and control, if CNOT) qubits
6:     Append gate  $a$  to circuit  $\mathcal{C}$ 
7:     Initialize parameters for new gate(s); retain previous optimized parameters
8:     Optimize all parameters of  $\mathcal{C}$  using COBYLA (fixed number of iterations)
9:     Evaluate cost  $C_t$  for current circuit
10:    if  $C_t < \zeta$  then
11:      break
12:    end if
13:  end for
14:  Record metrics (success/failure, gate count, circuit depth, absolute error)
15: end for

```

As demonstrated in [36], the random agent’s performance rapidly degrades with increasing problem size. The number of successful episodes (those that achieve the cost threshold) decreases sharply as the number of qubits grows. Moreover, even in successful cases, the random agent typically produces longer and less efficient circuits compared to reinforcement learning-based approaches. This underscores the necessity of leveraging reward feedback and adaptive strategies for scalable and efficient quantum architecture search.

C.4 SA-QAS: Simulated annealing for QAS

The algorithm leverages principles from simulated annealing to efficiently explore the space of possible quantum circuit architectures. The algorithm begins with an initial circuit populated with I gates (identity gates). At each iteration t , we perform the following steps:

1. Randomly select a position i in the circuit.
2. Replace the gate \mathbf{A}_i with the unitary matrix of a randomly selected quantum gate.
3. Calculate the change in the loss function: $\Delta L_t = L_t - L_{t-1}$.
4. Apply the acceptance criterion:
 - If $\Delta L_t < 0$ (improvement in loss), accept this change.
 - Otherwise, accept this change with probability $e^{-\Delta L_t/T_t}$, where $T_t = \alpha T_{t-1}$.

This process is repeated until either the loss remains stable for a predetermined number of iterations or the maximum iteration limit is reached. The final sequence of gates $\mathbf{A}_0, \dots, \mathbf{A}_{M-1}$ is submitted as our solution. The algorithm employs a geometric cooling schedule $T_t = \alpha T_{t-1}$. The initial temperature T_0 and the cooling rate α are both configurable hyperparameters that control the exploration-exploitation trade-off. Higher initial temperatures encourage more exploration early

in the search process, while the cooling rate determines how quickly the algorithm transitions to exploitation. The acceptance probability is defined as

$$P(\text{accept}) = \begin{cases} 1, & \text{if } \Delta L_t < 0 \\ e^{-\Delta L_t/T_t}, & \text{otherwise} \end{cases} \quad (13)$$

This probabilistic acceptance criterion is crucial for escaping local minima in the early stages of the search process, while gradually becoming more selective as the temperature decreases. SA-QAS terminates when either the loss function stabilizes (remains unchanged or changes below a threshold) for a predetermined number of consecutive iterations or the maximum iteration limit M is reached. Upon termination, the sequence of gates $\mathbf{A}_0, \dots, \mathbf{A}_{M-1}$ represents our discovered quantum circuit architecture.

In our implementation, we maintain a set of candidate quantum gates $\{\text{RX}, \text{RY}, \text{RZ}, \text{CNOT}\}$ from which random replacements are drawn. The loss function L quantifies how well the current circuit configuration performs on the target task. The specific form of the loss function depends on the quantum computational task being addressed. The hyperparameters T_0 and α significantly impact the search trajectory and should be tuned based on the specific problem characteristics.

D Noise modeling

Depolarizing noise model In our simulations, we model gate errors using the depolarizing noise channel, which provides a simple yet effective description of incoherent noise in quantum circuits [73]. For a single-qubit state ρ , the depolarizing channel is defined as

$$\mathcal{E}(\rho) = (1 - p)\rho + \frac{p}{2}I, \quad (14)$$

where p is the depolarizing error rate and I is the 2×2 identity matrix. This channel replaces the input state with the maximally mixed state $I/2$ with probability p , while leaving it unchanged with probability $1 - p$. For multi-qubit systems, the depolarizing channel generalizes to

$$\mathcal{E}(\rho) = (1 - p)\rho + p\frac{I}{2^n}, \quad (15)$$

where n is the number of qubits. In our experiments, we amplify the single-qubit and 2-qubit gate error rates to 10^{-2} and 5×10^{-2} , respectively, compared to currently available IBM Quantum [61] devices to assess the robustness of our algorithm. The depolarizing model is particularly suitable for capturing the average effect of noise in circuits with many gates, as it treats all Pauli errors as equally likely and leads to a simple, analytically tractable form of noise [73].

Shot noise Shot noise, also known as finite-sampling noise, is an intrinsic source of statistical uncertainty in quantum circuit measurements, arising from the quantum nature of measurement and the discrete, probabilistic outcomes inherent to quantum mechanics [74]. In quantum computing, the expectation values of observables are typically estimated by repeatedly executing a quantum circuit and recording the outcomes—a process referred to as collecting “shots”. Each shot yields a single outcome sampled from the underlying quantum probability distribution, and the aggregate of many shots provides an empirical estimate of the expectation value. However, due to the finite number of samples, this estimate is subject to statistical fluctuations that scale as $1/\sqrt{N}$, where N is the number of shots. This shot noise persists even in the absence of hardware errors and is governed by the Central Limit Theorem, which ensures that the distribution of the sample mean approaches a normal distribution as the number of shots increases [74]. While increasing the number of shots can reduce the variance of the estimate, practical constraints on quantum hardware often limit the feasible shot count, making shot noise a significant consideration in the design and analysis of quantum algorithms, especially for noisy intermediate-scale quantum (NISQ) devices.

E Robustness of TensorRL

E.1 More molecules

Table 4 provides a comparative analysis of TensorRL against both RL-based and non-RL-based quantum circuit ansatz discovery methods for finding ground states of 8-CH₂O and 10-CH₂O molecules.

Table 4: **TensorRL demonstrates robust performance by achieving ground state errors comparable to baseline RL, and other non-RL methods for QAS, while constructing quantum circuits with fewer gates and shallower depth.** Results are averaged over 5 random seeds for finding the ground state of 8-CH₂O and 10-CH₂O. For 10-CH₂O, the limited gate set RX, RY, RZ, CX prevents reaching the true ground state, indicating the need for more expressive gates (such as in ADAPT-VQE [16]).

Molecule	Method	Error	Depth	CNOT	ROT	Perform
8-CH ₂ O	TensorRL (trainable TN-init, $\chi = 2$)	8.0×10^{-5}	30	29	130	1
	TensorRL (zero angle)	7.6×10^{-5}	34	28	132	1
	TensorRL (fixed TN-init)	3.2×10^{-5}	16	13	22	1
	CRLQAS (rerun)	9.1×10^{-6}	43	60	31	1
	Vanilla RL	1.1×10^{-5}	56	44	61	0.9
	RA-QAS	1.3×10^{-3}	64	107	53	0.8
	SA-QAS	7.9×10^{-3}	35	59	28	0
10-CH ₂ O	TensorRL (fixed TN-init)	4.5×10^{-3}	15	26	37	0
	TensorRL (trainable TN-init, $\chi = 3$)	4.3×10^{-3}	39	43	163	0
	TensorRL (trainable TN-init, $\chi = 2$)	6.1×10^{-3}	34	41	165	0
	StructureRL	4.7×10^{-3}	34	36	169	0
	CRLQAS (rerun)	4.2×10^{-3}	34	43	23	0
	Vanilla RL	4.3×10^{-3}	344	193	157	0
	RA-QAS	6.7×10^{-3}	179	354	120	0
	SA-QAS	8.0×10^{-3}	38	70	23	0

See Appendix. G.3 for the molecular configuration details. The results demonstrate that TensorRL consistently achieves errors on the same order of magnitude as strong baselines (e.g., CRLQAS, Vanilla RL), while often constructing quantum circuits with significantly fewer gates and reduced depth.

For 8-CH₂O, the *TensorRL (fixed TN-init)* variant achieves a notably low error (3.2×10^{-5}) with the shallowest circuit (depth 16) and the fewest CNOT and rotation gates among all tested methods, highlighting its efficiency. For 10-CH₂O, although none of the methods reach the true ground state due to a restricted gate set, *TensorRL (fixed TN-init)* still constructs the shallowest circuit (depth 15) with a competitive error (4.5×10^{-3}), outperforming other methods in circuit compactness. The experiments also reveal that methods relying solely on the RX, RY, RZ, CX gate set are limited in expressivity for larger molecules, suggesting the need for more expressive gates (as in ADAPT-VQE [16]) to achieve ground state accuracy for challenging systems.

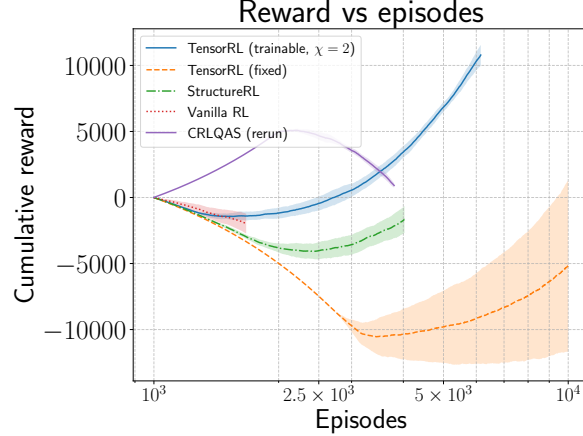
In summary, Table 4 highlights the robustness and efficiency of TensorRL, particularly its *fixed TN-init* variant, in constructing compact quantum circuits while maintaining competitive accuracy compared to both RL and non-RL baselines. These results underscore TensorRL’s potential for scalable and resource-efficient quantum circuit discovery in quantum chemistry applications.

E.2 Reward signal analysis

Figure 4 presents the cumulative reward as a function of training episodes for all evaluated methods: TensorRL (trainable, $\chi = 2$), TensorRL (fixed), StructureRL, Vanilla RL [21], and CRLQAS [34] (rerun). The x -axis is shown on a logarithmic scale to highlight both early and late training dynamics.

- **TensorRL (trainable, $\chi = 2$):** This method demonstrates the strongest performance, with cumulative rewards increasing rapidly after approximately 2.5×10^3 episodes. By the end of training, it achieves the highest cumulative reward, exceeding 10,000, and exhibits low variance, indicating stable and effective learning.
- **TensorRL (fixed):** While this variant outperforms StructureRL and Vanilla RL, its cumulative reward plateaus at a lower value compared to the trainable version. This suggests that trainable parameters in TensorRL are critical for achieving superior performance.

Figure 4: **Cumulative reward vs. episodes for all evaluated methods in the task of finding the ground state of 8-H₂O.** All methods are trained for ~ 48 hours, and the shaded regions represent the standard deviation across runs. *TensorRL (trainable $\chi = 2$)* shows a sharp increase in accumulated reward compared to other methods, showing enhanced trainability. The shaded area in the plot corresponds to the standard deviation (σ) from the average over 5 random initializations of the neural network.



- **StructureRL:** This method shows moderate improvement, with cumulative rewards remaining positive but not reaching the levels of either TensorRL variant. The variance is also relatively contained, suggesting consistent, albeit limited, learning progress.
- **Vanilla RL:** The baseline method struggles to achieve significant positive rewards, with its curve remaining near zero throughout training. This highlights the difficulty of the task and the necessity of structural enhancements.
- **CRLQAS (rerun):** This method initially suffers a sharp decline in cumulative reward, reaching values below $-10,000$ around 5×10^3 episodes. While some recovery is observed, the method remains substantially below the others in final performance and exhibits high variance.

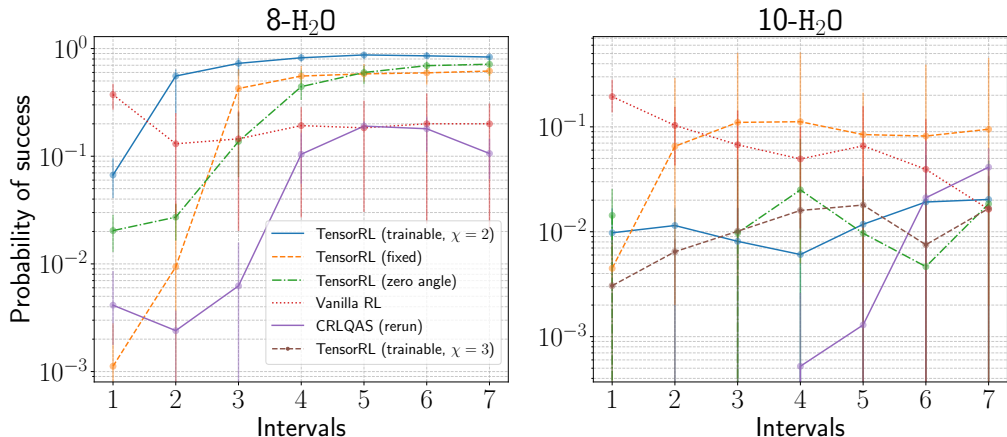
Overall, these results demonstrate that the proposed TensorRL (trainable) approach significantly outperforms baseline and alternative methods, both in terms of final cumulative reward and learning stability. The advantage of trainable structure within the RL framework is particularly evident, as fixed or less-structured baselines lag in both reward magnitude and convergence speed.

E.3 Success rate with scaling

Here we investigate Fig. 5, where we plot the probability of success of finding a parameterized quantum circuit that finds the ground state of 8- and 10-H₂O molecules with an increasing number of episodes. The results are summarized in the following:

- **TensorRL (fixed) performance** For 8-H₂O: Starts with low success ($\sim 0.1\%$) but steadily improves to approximately 50%. The performance curves shown represent maximum and minimum values over 5 random neural network initializations, demonstrating robust training stability. For 10-H₂O: While the average success probability remains around $\sim 10\%$, the maximum reaches an impressive 50% success rate for some initializations. This significantly outperforms other methods, which struggle to reach even 1% success at this qubit scale. Exhibits only a $\sim 5:1$ performance reduction when scaling up from 8- to 10-qubit. Preserves reasonable success rates at larger scales, making it valuable for practical applications.
- **CRLQAS comparison** For 8-H₂O: Begins with extremely low success ($\sim 0.3\%$) and improves to $\sim 10\text{-}20\%$, with visible variability across different initializations. For 10-H₂O: Reaches only $\sim 5\%$ at its maximum performance across initializations, despite showing

Figure 5: **The probability of finding a successful episode i.e. a quantum circuit that finds the ground state of 8-, 10-H₂O consistently increases with TensorRL (fixed).** The error bar represents maximum and minimum values across 5 random neural network initializations, highlighting the robustness of TensorRL (fixed) even at its worst initialization compared to other methods.



an upward trajectory. Even at its best initialization, CRLQAS fails to approach the 50% maximum success rate achieved by TensorRL (fixed). Shows better scaling properties than trainable models but still substantially underperforms TensorRL (fixed) across all initialization. Demonstrates potential for continued improvement with additional training, but lags significantly behind TensorRL (fixed) in maximum achievable performance.

- **Vanilla RL performance** For 8-H₂O: Starts with moderate performance ($\sim 30\%$) but consistently declines across all initialization. For 10-H₂O: Shows continuing performance degradation over time with success rates below 5% for all initializations, never approaching the 50% maximum achieved by TensorRL (fixed). Ultimately falls below TensorRL (fixed) for both system sizes at all initialization configurations. Highlights the limitations of non-tensor-based approaches for quantum circuit optimization, with even its best initialization performing poorly compared to TensorRL (fixed).

TensorRL (fixed)’s average $\sim 10\%$ success probability for 10-qubit systems (with maxima reaching 50% across initializations) means up to half of optimization episodes can yield useful circuits in optimal configurations. This substantially reduces computational overhead for practical quantum simulations. No other method demonstrates this level of success at the 10-qubit scale, with most failing to exceed 1% success rate even at their best initialization. The constrained parameter space of fixed models avoids overfitting while maintaining expressivity. TensorRL (fixed) demonstrates the best capability for representing complex quantum correlations at scale, with its worst initialization often outperforming the best initializations of alternative methods. The consistent 50% maximum success probability for 10-qubit systems provides unprecedentedly efficient circuit discovery for moderately sized molecules, representing a significant advancement for Hamiltonian ground state estimation.

E.4 TensorRL on CPU

Our experimental results, summarized in Figure 6, demonstrate that TensorRL in trainable mode on CPU achieves training efficiency that is competitive with, and often superior to, established baselines such as CRLQAS and vanilla RL operating on GPU. For quantum architecture search tasks up to 8-qubit, TensorRL (trainable, CPU) consistently matches or outperforms the GPU-based baselines in terms of wall-clock time per episode and per successful episode. Notably, this improvement in computational efficiency does not come at the expense of solution quality: the minimum number of gates required to reach chemical accuracy is comparable to, or slightly better than, those achieved by the baselines. These results establish that RL-QAS, when implemented with TensorRL, is practically

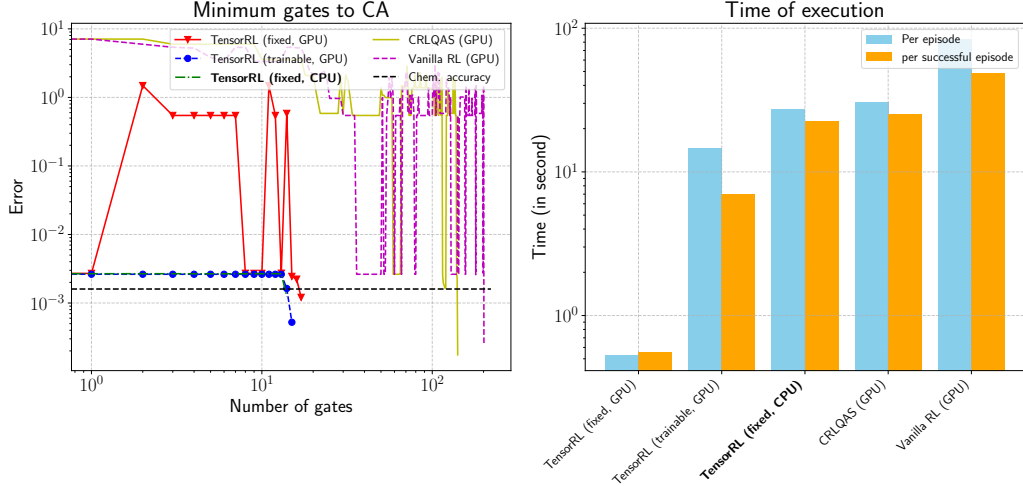


Figure 6: **Comparison of training time and circuit efficiency for TensorRL (fixed CPU/GPU) versus CRLQAS (GPU) and vanilla RL (GPU):** TensorRL (fixed, CPU) achieves up to 10 \times fewer gates to chemical accuracy and matches or surpasses GPU-based baselines in training time, enabling efficient and accessible quantum architecture search on standard CPUs. Here CA denotes the chemical accuracy.

trainable on standard CPUs for problem sizes up to 8-qubit, significantly broadening accessibility to high-quality quantum circuit design without reliance on specialized hardware.

E.5 TensorRL-QAS beyond chemical Hamiltonians

Table 5 presents a comprehensive comparison of TensorRL and TF-QAS [41] on non-chemical Hamiltonian problems, specifically the 5-qubit Heisenberg model and the 6-qubit transverse field Ising model (TFIM) (with magnetic field strength $h = 5 \times 10^{-2}$). The Hamiltonians for these models are defined as

$$H_{\text{TFIM}} = \sum_{i=1}^n Z_i Z_{i+1} + h \sum_i X_i, \quad (16)$$

and

$$H_{\text{Heis}} = \sum_{i=1}^n X_i X_{i+1} + Y_i Y_{i+1} + Z_i Z_{i+1} + \sum_{i=1}^n Z_i, \quad (17)$$

where n denotes the number of qubits. Across both models, TensorRL demonstrates clear advantages

Table 5: **TensorRL variants outperform TF-QAS [41] on finding the ground state of the 5-qubit Heisenberg model and the 6-qubit transverse field Ising model (TFIM).** It should be noted that TF-QAS utilizes a gateset that consists of $\{XX, YY, ZZ\}$ along with 1-qubit rotations that should be transpiled to compare fairly to the numbers presented for TensorRL. NA denotes Not Available.

Problem	Method	Error	Depth	CNOT	GATE
5-Heisenberg	TensorRL (fixed TN-init)	7.6×10^{-2}	15	5	33
	TensorRL (trainable TN-init, $\chi = 2$)	3.7×10^{-4}	46	28	127
	StructureRL	2.6×10^{-3}	48	33	127
	TF-QAS	1.2×10^{-3}	NA	NA	35
6-TFIM	TensorRL (fixed TN-init)	2.4×10^{-4}	13	13	22
	TensorRL (trainable TN-init, $\chi = 2$)	1.8×10^{-6}	29	16	111
	StructureRL	1.8×10^{-6}	34	20	116
	TF-QAS	1.4×10^{-12}	NA	NA	36

in circuit efficiency and solution accuracy. For the 5-qubit Heisenberg model, TensorRL with fixed tensor network initialization achieves the lowest gate count (33 gates) and a competitive error of 7.6×10^{-2} , while the trainable TN-init variant further reduces the error 3.7×10^{-4} , outperforming StructureRL and TF-QAS in accuracy, albeit with increased circuit depth and gate count. Similarly, for the 6-qubit TFIM, TensorRL with fixed TN-init yields the most compact circuit (22 gates) and low error (2.4×10^{-4}), while the trainable variant matches the best error (1.8×10^{-6}) achieved by StructureRL, but with fewer gates and reduced depth. Although TF-QAS attains the lowest error for TFIM, it lacks detailed circuit complexity metrics and does not consistently outperform TensorRL in gate efficiency. These results highlight that TensorRL not only excels in quantum chemistry but also provides state-of-the-art performance for general quantum many-body Hamiltonians, constructing compact and accurate circuits and demonstrating its versatility and robustness beyond chemical applications.

E.6 Scaling beyond 12-qubits

We examine the scalability of TensorRL-QAS and discuss its current limitations. To assess scalability, we consider transverse field Ising models of 15, 17, and 20 qubits, with the Hamiltonian defined in Eq. 16 and a magnetic field strength of $h = 10^{-3}$. As established in Section 3 and Section 6, the *TensorRL (fixed)* variant yields the lowest computational overhead per reinforcement learning (RL) episode. Therefore, we adopt this method to evaluate scalability across increasing system sizes. Our

Table 6: **Scalability analysis of TensorRL-QAS for approximating ground-state energies of 15-, 17-, and 20-qubit transverse-field Ising models (TFIM) with weak magnetic field ($h = 10^{-3}$).** Results demonstrate up to 21% energy improvement over initial MPS states for systems ≤ 17 qubits (errors $\sim 10^{-4}$), while the 20-qubit case reveals limitations due to restricted bond dimensions ($\chi = 2$) and action-space expressivity.

Problem	Method	Error	Improvement
15-TFIM	TensorRL (fixed TN-init)	4.4×10^{-4}	21%
17-TFIM		4.8×10^{-4}	19%
20-TFIM (bottleneck)		6.7×10^{-4}	1%

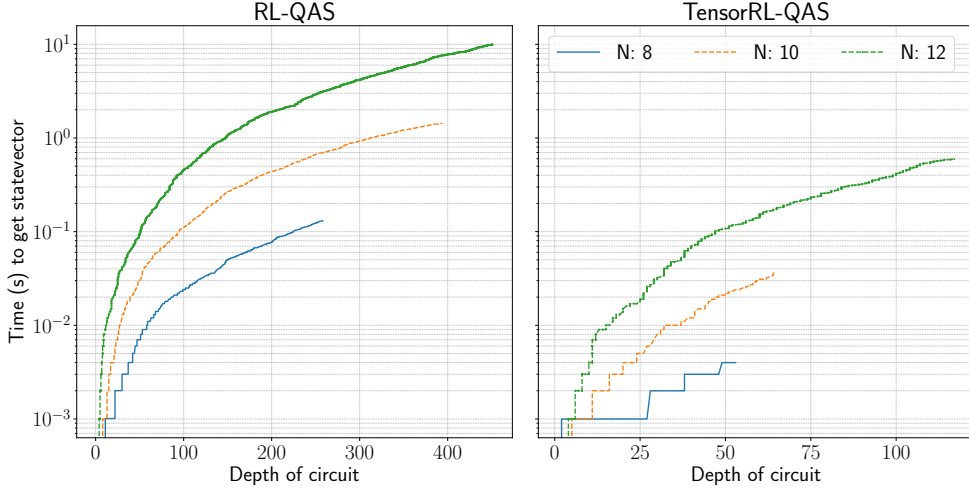
results, summarized in Table 6, demonstrate that TensorRL-QAS yields accurate approximations of the ground state energy for the TFIM up to 17 qubits. Specifically, the method improves the energy by up to 19% relative to the initial MPS state, achieving approximation errors of 4.5×10^{-4} for the 15-qubit system and 4.8×10^{-4} for the 17-qubit system. For the 20-qubit case, while the approximation error remains low at 6.7×10^{-4} , the improvement over the warm-started MPS state is limited to just 1%. This suggests that the current action space, the brickwork circuit structure, and the restricted MPS bond dimension ($\chi = 2$ in our experiments) constrain further progress. Enhanced performance may be attainable by employing MPS with larger bond dimensions and adopting a more expressive action space, as explored in ref. [16].

F Scalability bottlenecks: Analysis of quantum simulator

The Fig. 7 presents a critical comparison between baseline reinforcement learning-assisted quantum architecture search (RL-QAS) and tensor network (TN) for RL-QAS (TensorRL-QAS) approaches, revealing fundamental scalability challenges in quantum computing. As depicted in the left panel, the baseline RL-QAS method exhibits a severe computational bottleneck where statevector calculation time increases exponentially with both circuit depth and qubit count. For a system with $N = 12$ qubits, computation time reaches approximately 10 seconds at circuit depths approaching 400, while even modest depths with $N = 8$ qubits require significantly less time (approximately 0.1 seconds at depth 200). This exponential scaling represents a fundamental limitation to practical quantum applications.

A crucial consideration for real-world implementation is that reinforcement learning agents typically require multiple episodes to converge to optimal policies. If training necessitates an average of 10,000 episodes, as is common in complex RL tasks, the total computation time for RL-QAS becomes entirely intractable. With each episode requiring up to 10 seconds of statevector calculation for

Figure 7: **Time taken by Qulacs [75] simulator to get the statevector with baseline RL-QAS and TensorRL-QAS methods with varying numbers of qubits and depths of circuit.** The substantial difference in computation time becomes even more critical when considering that training requires approximately 10,000 episodes, making RL-QAS approaches intractable for larger qubit systems.



$N = 12$ qubits, the complete training process could require approximately 100,000 seconds (over 27 hours) of computation time solely for statevector calculations. This computational burden effectively precludes scaling to larger, more practical quantum systems where 12+ qubits would be required.

In stark contrast, the right panel demonstrates TensorRL-QAS's superior performance characteristics. TensorRL-QAS requires substantially shallower circuits to achieve comparable results, with maximum depths of only about 100 compared to 400 for baseline methods. More importantly, computation times remain under 0.5 seconds even for $N = 12$ qubits, reducing the projected training time for 10,000 episodes to approximately 5,000 seconds (less than 1.5 hours). This dramatic improvement stems from TensorRL-QAS's innovative "warm start" approach, which leverages matrix product states (MPS) for parameterized quantum circuit (PQC) initialization.

The warm start strategy enables TensorRL-QAS to converge to solutions in significantly fewer steps, creating a computational advantage that increases with qubit count. By effectively mapping the tensor network representation to quantum circuit parameters, TensorRL-QAS addresses one of the primary obstacles in quantum machine learning scalability. This initialization method bypasses the exponential growth in statevector computation time that plagues conventional approaches, making TensorRL-QAS substantially more suitable for practical quantum applications requiring larger qubit systems.

The logarithmic scale in the figure clearly illustrates the magnitude of this advantage, with the baseline method showing steep growth curves across all qubit counts. At the same time, TensorRL-QAS maintains relatively modest computation times even as system size increases. These results strongly suggest that tensor network initialization strategies represent a promising direction for overcoming limitations in quantum machine learning approaches, potentially enabling quantum advantage in practical applications that would otherwise remain computationally intractable using conventional methods.

G Experimental setup

G.1 Reward function

We employ the reward function R from [21, 34] with modifications for quantum tasks:

$$R = \begin{cases} 5, & \text{if } C_t < \xi \\ -5, & \text{if } t \geq T_s^e \text{ \& } C_t \geq \xi \\ \max\left(\frac{C_{t-1} - C_t}{C_{t-1} - C_{\min}}, -1\right), & \text{otherwise} \end{cases} \quad (18)$$

where $C_t = \langle 0|U^\dagger(\boldsymbol{\theta})HU(\boldsymbol{\theta})|0\rangle_t$ represents the variational energy at step t , ξ is a precision threshold, and T_s^e denotes the episode’s step limit. The ± 5 rewards terminate episodes upon success (energy $< \xi$) or failure (timeout with energy $\geq \xi$).

For quantum chemistry tasks, the threshold ξ is typically set to 1.6×10^{-3} as it defines the precision such that realistic chemical predictions can be made. The goal of the agent is to obtain an estimated value of C_{\min} within such precision. Whereas, while solving the Heisenberg model, we consider ξ to 10^{-3} and for the transverse field Ising model we set it as 10^{-2} , which are obtained by running SA-QAS [38] on these Hamiltonians.

Table 7: **Steps per episode** required for convergence to ground energy.

Qubits	TensorRL-QAS	CRLQAS	RAQAS
6	20	70	97
8	20	250	300
10	20	350	477
12	40	450	450
15	60	NA	NA
17	60	NA	NA
20	80	NA	NA

G.2 Agent-environment specifications

Our implementation leveraged the double deep-Q network (DDQN) algorithm with $n = 5$ step trajectory roll-outs [76], employing a discount factor $\gamma = 0.88$ and ϵ -greedy exploration where ϵ decays geometrically from 1 to 0.05 (decay rate 0.99995/step). The target network updated every 500 steps, with unified hyperparameters across quantum systems: batch size 1000, replay memory capacity 20,000, ADAM optimizer [57] ($\eta = 3 \times 10^{-4}$), and 5-layer neural networks (1000 neurons/layer). All TensorRL configurations used bond dimension $\chi = 2$ unless explicitly varied, maintaining consistent entanglement patterns throughout the architecture search process. The number of steps (i.e. maximum number of gates allowed to add) per episode is provided in Tab. 7, which shows that TensorRL-QAS requires less than half of the number of steps per episode for QAS tasks.

G.3 Molecular configuration

Using the Born-Oppenheimer approximation, we fix a finite basis set, in our case STO-3G, for all the molecules except 10-H₂O, where we use 6-31G to extend the number of orbitals and to discretize the system. We choose the molecules based on the top 20 molecules provided by PennyLane [58], and throughout the paper, we use PennyLane along with OpenFermion to generate the chemical Hamiltonians in Tab. 8.

G.4 MPS to PQC conversion gate resources

In Tab. 9 we present the resources in the one-depth brickwork structure required when converting from MPS to parameterized quantum circuit. The resources are quantified by the number of CNOTs, rotations (ROT) and depth (Depth) of the circuit and in the case of 10-qubit, the bond dimension χ . All the circuits are simulated using Qulacs [75].

Table 8: **The geometry and basis of molecules used in this research.** The coordinates is in Angstrom units.

Molecule	Geometry	Basis
6-BEH ₂	H (0,0,-1.33); Be (0,0,0); H (0,0,1.33)	STO-3G
8-H ₂ O	H (-0.02,-0,0); O (0.84,0.45,0); H (1.48,-0.27,0)	STO-3G
8-CH ₂ O	C (0,0,0); H (1.08,0,0); H (-0.23,1.06,0)	STO-3G
10-H ₂ O	H (-0.02,-0,0); O (0.84,0.45,0); H (1.48,-0.27,0)	6-31G
10-CH ₂ O	C (0,0,0); H (1.08,0,0); H (-0.23,1.06,0)	STO-3G
12-LiH	Li (0,0,0); H (0,0,3.40)	STO-3G

Table 9: **Gate counts and depth for MPS-to-circuit conversion across different system sizes.** The number of gates increases with bond length χ .

Qubits	CNOT	Depth	ROT
5 ($\chi = 2$)	12	27	75
6 ($\chi = 2$)	15	27	93
8 ($\chi = 2$)	21	27	129
10 ($\chi = 2$)	27	27	165
10 ($\chi = 3$)	26	27	160
12 ($\chi = 2$)	33	27	201
15 ($\chi = 2$)	42	27	255
17 ($\chi = 2$)	48	27	291
20 ($\chi = 2$)	57	27	345

H Computed resources

We utilize a system with an AMD Rome 7H12 CPU based on AMD Zen 2 architecture and an Nvidia Ampere A100 GPU. The time of training and approaching the first and minimum error is presented in Tab. 10, all times are noted in hours. For all the configurations, we utilized 2 CPUs, each with a maximum 4GB memory and maximum 40 GB GPU memory.

Table 10: **The training time for different TensorRL-QAS methods across various qubits.** We notice that *TensorRL (fixed)* converges much faster to the desired error than other methods.

Method / Metric (in hours)	5q	6q	8q	10q	12q
TensorRL (fixed)					
Time to min error	5.88	0.05	0.91	11.22	0.58
Time to first success	5.24	0.05	0.15	0.53	0.58
Total train time	6.42	0.13	1.48	34.82	48.00
TensorRL (trainable)					
Time to min error	6.14	0.24	27.60	0.56	48.15
Time to first success	6.14	0.02	0.40	0.56	17.07
Total train time	29.84	2.00	40.84	47.50	48.00
StructureRL					
Time to min error	5.42	0.66	35.47	23.92	14.86
Time to first success	5.42	0.27	1.03	23.92	4.81
Total train time	29.84	1.91	45.75	47.69	48.00